stages might be produced by cooperative activity of ER and ribosomes. These inclusion-like structures with abnormal accumulation of ER seemed likely to represent a precursor to the later neuronal LBHI observed in this line. These results imply that the deterioration of ER function and the involvement of ER might be important for formation and developing neuronal LBHI/Ast-HI in mutant SOD1 harboring FALS patients.

DISCUSSION

Aggregated proteins or inclusions are a pathological hallmark and possible causative agent of several neurodegenerative disorders including ALS [39]. While LBHI/Ast-HI have been established as morphological hallmarks of mutant SOD1-linked FALS, little is known about the formation of these structures in neurons [6]. Several in vitro systems have been provided for analysis mutant SOD1 aggregation [35,36,40], however, the relationship between mutant SOD1 aggregation *in vitro* and pathological hyaline inclusions *in vivo* remains unclear. The LHI we observed in SK-N-SH cells expressing mutant SOD1 provide a direct link between *in vitro* and *in vivo* SOD1 aggregation. To our knowledge, this is the first study to show reproducible induction of LBHI/Ast-HI like structures meeting the criteria of inclusion bodies [24,26,31,38,41].

LBHIs/Ast-HIs in human FALS consist of a chaotic mixture of cytoplasmic proteins (such as SOD1, copper chaperone for SOD (CCS), peroxiredoxin 2, and glutathione peroxidase 1), cytoskeletal proteins (such as tubulin, tau protein, and phosphorylated- and nonphosphorylated neurofilament), nuclear proteins (such as neuron-specific enolase) and synaptic proteins (such as synaptophysin [24,38,41–43]). Recently, it has been published that GRP78/BiP, an ER resident chaperon protein, is also co-localized with LBHI of G93A SOD1 mice [28]. GRP78/BiP is molecular chaperone protein induced by IRE1 in response to aberrant protein folding and promotes proper protein folding. In this context, GRP78/BiP may be acting as part of the UPR response to resolve granule coated fibrils. Tobisawa et al. [35] reported increased protein levels of GRP78/BiP in motor neurons of mutant SOD1 transgenic mice, suggesting that the motor neurons in their model suffer from 'ER stress'. While the importance of ER stress or proteosome malfunction in formation of mutant SOD1 aggregates has been established [35,36,40], the mechanisms by which mutant SOD1 forms LBHI/Ast-HI in FALS remain poorly understood. In this study, we present three lines of evidence for the involvement of ER stress in early events in LBHI/Ast-HI formation. First, ER stress in neuroblastoma cells expressing mutant SOD1 results in SOD1- and ubiquitin-immunopositive LHIs, compatible with LBHI/Ast-HI, composed of granule-coated fibrils approximately 15–25 nm in diameter and granular materials (Figs. 5 and 6). Secondly, we observed similar structures in the spinal cord of L84V SOD1 transgenic mice at pre-symptomatic stages, including abnormal electron dense, i.e. stressed, ER and numerous free ribosomes. (Figs. 4 and 7). Third, positive staining against anti-KDEL antibody, which recognizes ER resident proteins such as calreticulin, GRP 94, PDI and GRP78/BiP, were observed in both the LHI and Ast-HI of L84V SOD1 transgenic mice at symptomatic stages (Fig. 6E–H). These findings support the hypothesis that ER stress induces LBHIs/Ast-HIs creation in FALS patients with mutant SOD1. Taken together, these observations suggest that LHI in neuroblastoma cells and LBHI/Ast-HI in FALS patients might develop through similar processes.

In this study, we presented evidences that ER stress causes aggregates of mutant SOD1 and formation of LHI which is compatible with LBHI/Ast-HI. However, other questions arise from these results. 1) Why did same stress induce the different outcome of mutant SOD1 aggregation in the neuroblastoma? 2) Are the smaller aggregates competent to develop to LHIs? To answer these questions, we sought without success to identify the origin of the granule coated fibrils or SOD1 containing filamentous structure (e.g. less densely coated fibrils) in the smaller SOD1 aggregates localized to ER in L84V SOD1 expressing cells. Nevertheless, we found common features between the small aggregates in L84V SOD1 expressing SK-N-SH cells and neuronal LBHI-precursor in L84V transgenic mice, including regions of abnormal ER aggregation surrounded by abundant free ribosomes (Fig. 4B and Fig 7C). Furthermore, LHI and Ast-HI were immunopositive for the KDEL peptide present in ER-resident proteins, suggesting the involvement of ER itself in formation or development of LBHI/Ast-HI (Fig. 6E–H). We suggest that aberrant SOD1 fibril might be produced by cooperative activity of ER and ribosomes. To answer the questions, careful observation of LHI with time lapse analysis is needed.

It remains unclear why the major symptoms of ALS in patients with mutant SOD1-linked FALS do not develop until middle age, but we speculate that age-dependent changes in responses to ER stress might provide an answer. Under normal conditions, newly synthesized and misfolded proteins are refolded by chaperons such as GRP78, 94, calnexin, and calreticulin. This UPR response may be more robust in younger FALS patients and might be the reason the proteins aggregates are not observed in young patients even though mutant SOD1 is expressed. However, a decrease in protein folding or chaperone capability may occur with aging, and accumulation of misfolded proteins in the ER lumen may gradually lead to ER stress [44]. Consistent with this idea, Tobisawa et al. reported mutant SOD1 retention in the ER in COS7 cells [35] and Kikuchi et al. reported age-dependent increase of mutant SOD1 aggregation to ER in spinal cord of G93A SOD1 mice, suggesting ER dysfunction might be caused by mutant SOD1 [36]. Prolonged ER stress associated with insufficient degradation of misfolded proteins would subsequently activate apoptotic pathways. Nakagawa et al. reported that caspase-12, the ER resident caspase, is specifically cleaved and activated by ER stress, and that cells derived from mice lacking caspase-12 are resistant to ER stress [16]. In the spinal cords of G93A SOD1 mice, caspase-12 is activated in symptomatic period and can be inhibited by overexpression of XIAP (X-linked inhibitor of apoptosis protein [45,46]. Then, we analyzed activation of caspase-4 (the human orthologue of rodent caspase-12) following tunicamycin treatment. As expected, the SOD1 aggregates of the L84V SOD1-expressing neuroblastoma cells colocalized with caspase-4 (unpublished data), implying caspase-4 might contribute to cell death in our model system.

Although it can take longer than 30 years for LBHI/Ast-HI to develop in FALS patients, we could induce the formation of morphologically similar LHI within 24 hours in our simple model. Detection of the molecular targets for ER stress-induced hyaline inclusions of mutant SOD1 in our model might lead to the development of therapy that can prevent the progression of mutant SOD1-linked FALS. Ultimately, our study should contribute to the development of a simple system to analyze novel therapies for ALS.

MATERIALS AND METHODS

Transgenic Mice

Transgenic mice for mutant human SOD1^{L84V} (C587BL/6 background) were created (M. Kato, et al. Transgenic mice with ALS-linked SOD1 mutant L84V. Abstract of the 31st Annual Meeting of Society for Neuroscience, San Diego, 2001). Mice were genotyped by PCR to detect the mutant SOD1 transgene using

the following primers: forward, TTGGGAGGAGGTAGTGATTA; reverse, GCTAGCAGGATAACAGATGA. The onset of symptoms was at 5–6 months and the initial sign of the disease was usually weakness in their hindlimbs, while approximately 10% of the mice first showed weakness in their forelimbs.

Chemicals and antibodies

We used the following antibodies: anti-SOD1 polyclonal antibody (pAb; Chemicon, Temecula, CA); anti-ubiquitin pAb and anti-KDEL mAb (Stressgen, Victoria, BC. Canada); anti-Tim17 pAb and anti-Tom20 pAb (grateful gifts by Dr. Otera and Prof. Mihara [47,48]); Alexa Fluor 488-conjugated anti-sheep IgG, Alexa Fluor 588-conjugated anti-mouse IgG antibody, and Alexa Fluor 588-conjugated anti-rabbit IgG antibody (Molecular Probes, Eugene OR); biotinylated anti-sheep IgG (Vector Laboratories, Burlingame, CA); anti-FLAG mAb (Sigma, woodlands, USA); anti-myc pAb and anti-GFP-mAb (Santa Cruz, Santa Cruz, CA); HRP-conjugated anti-sheep IgG (Jackson ImmunoResearch Laboratories Inc., West Grove, PA); and HRP-conjugated anti-mouse IgG and HRP-conjugated anti-rabbit IgG antibody (Cell Signaling Technology, Beverly, MA). Tunicamycin was obtained from Sigma.

Cell culture and induction of ER stress

SK-N-SH human neuroblastoma cells were obtained from the Riken Cell Bank (Tsukuba, Japan), and were cultured in α-MEM (Invitrogen) containing 10% fetal bovine serum at 37°C under 5% CO_2. These cells were transfected with pcDNA3.1-hSOD1 and pcDNA3.1-hL84V-SOD1 to cause overexpression of wild-type or L84V mutant SOD1, respectively. G418 resistant stable neuroblastoma cell lines expressing equal levels of endogenous and exogenous SOD1 were established. In all experiments, we used cultures that were at 70–80% confluence to avoid the influence of stress induced by overgrowth. On the day of stimulation, fresh medium was added more than 1 h before exposure to stress in order to ensure the same conditions for each culture.

Western blot analysis

SK-N-SH cells stably expressing wild-type or L84V SOD1 were washed with PBS, harvested, and lysed in TNE buffer containing 1 mM PMSF and 1% SDS. 10 μg of protein was subjected to 12% SDS-PAGE and transferred to a PVDF membrane (Millipore Corp.). The membrane was blocked with 5% skim milk and incubated with anti-SOD1 antibody (1:1500 dilution), followed by incubation with an HRP-conjugated secondary antibody. Proteins were visualized with an ECL detection system (Amersham-Pharmacia).

Immunocytochemistry

SK-N-SH cells stably expressing wild-type SOD1 or L84V SOD1 were treated with 1 μg/ml of tunicamycin for 24 h. Then the cells were fixed with Zamboni's solution (0.1 M phosphate-buffered saline (PBS; pH 7.4) containing 2% paraformaldehyde (PFA) and 21% picric acid), rinsed in 0.1 M PBS, and incubated for 30 min in 0.3% H_2O_2 to eliminate endogenous peroxidases. Next, the cells were incubated overnight at 4°C with the primary antibody (a polyclonal sheep anti-SOD1 antibody; Calbiochem) at 1:1000 in 0.1 M PBS containing 0.3% Triton X-100 and 3% bovine serum albumin (BSA). After washing in 0.1 M PBS, cells were incubated for 30 min with the secondary antibody (biotinylated anti-sheep IgG) (Vector Laboratories). After amplification with avidin-biotin complex from the ABC kit (Vector Laboratories), reaction products were visualized with 0.05 M Tris-HCl buffer (TBS; pH 7.6) containing 0.02% diaminobenzidine tetrahydrochloride (DAB) and 0.01% hydrogen peroxide. Finally, the cells were counterstained with Mayer's hematoxylin and eosin (HE).

Co-immunoprecipitation assay utilizing ubiquitin

Lysates of pcDNA3.1-myc-tagged ubiquitin (a kind gift from Dr. Niwa and Prof. Sobue [32])-transfected SK-N-SH cells stably expressing wild-type SOD1 or L84V SOD1 were prepared using TNE buffer (10 mM Tris-HCl, (pH 7.4), 150 mM NaCl, and 1 mM EDTA) containing 1 mM phenylmethylsulphonyl fluoride (PMSF), 2 μg/ml aprotinin, and 1% Nonidet P-40 after treatment with or without 4 μg/ml ALLN for 12 h. Then, 1 μg of anti-FLAG antibody was added to 400 μg of lysate, followed by incubation at 4°C for at least 3 h. Protein G-Sepharose (10 μl gel) was then added and incubation was done with rotation at 4°C for 1 h. The immunoprecipitate was subjected to SDS-PAGE and transferred to a polyvinylidene fluoride (PVDF) membrane. The membrane was blocked with 5% skim milk and then was incubated with anti-Myc antibody (1:1000 dilution), followed by incubation with an HRP-conjugated secondary antibody. Proteins were visualized with an ECL detection system (Amersham-Pharmacia).

Immunofluorescence and chemifluorescence

SK-N-SH cells expressing wild-type SOD1 or L84V SOD1 were incubated with or without tunicamycin or ALLN, rinsed in 0.02 M PBS, and fixed in Zamboni's fixative. Then the cells were incubated overnight at 4°C with an anti-SOD1 antibody (1:1000 dilution) and either anti-KDEL (1:500 dilution), anti-GM130 (1:500 dilution) or anti-ubiquitin (1:500 dilution) antibody in 0.02 M PBS containing 0.3% Triton X-100 and 3% BSA. Next, the cells were treated with fluorescent dye (Alexa Fluor 488)-conjugated donkey anti-sheep IgG (SOD1; 1:1000 dilution), fluorescent dye (Alexa Fluor 568)-conjugated goat anti-mouse IgG (KDEL, GM130; 1:1000 dilution), and goat anti-rabbit IgG (ubiquitin; 1:1000) as the secondary antibodies for 1 h at RT in 0.02 M PBS containing 3% BSA. Examination was done under a Zeiss LSM 510 microscope. For detection of SOD1 colocalization with cytochrome b5, pCMV b5-EGFP vector was transfected to the cells (kind gift from Dr. Otera and Prof. Mihara; [49]). The GFP signal was enhanced by anti-GFP antibody staining (1:100). In order to determine the localization of SOD1 in living cells, SK-N-SH cells expressing wt and L84V SOD1 were transfected with a pcDNA3.1-GFP-tagged wt and L84V SOD1 plasmid, respectively. After treatment with tunicamycin for 24 hr, the cells were further incubated with Mito-tracker or Lyso-tracker (Molecular Probes) for 30 min to visualize the mitochondria or lysosomes, respectively. Then the cells were rinsed at least three times in 0.1 M PBS and fixed with Zamboni's solution for examination under a LSM 510 confocal microscope (Zeiss, Osaka, Japan).

Electron microscopy

SK-N-SH cells stably expressing L84V SOD1 were exposed to 1 μg/ml tunicamycin for 24 h and then fixed at room temperature (RT) for 1 h in 0.1 M phosphate buffer (PB) containing 2.5% glutaraldehyde (GA) and 2% paraformaldehyde. Subsequently, the cells were post-fixed in 1% OsO_4 at RT for 1 h, dehydrated in a graded ethanol series, and embedded in epoxy resin (Quetol 812; Nisshin EM Co.). Areas containing cells with aggregates were block-mounted in epoxy resin by the direct epoxy-resin embedding method and cut into 90-nm sections. The sections were counterstained with uranyl acetate and lead citrate, and then examined using an H-7100 electron microscope (Hitachi).

Immune Electron microscopy

As with immunocytocemistry methods above, after fixation with Zamboni solution containing 0.1% GA, the cells with anti-SOD1 antibody were developed with DAB. Then, they were post-fixed in 1% OsO4 in 0.1 M PB at RT for 30 min after 1% GA in 0.1M PB re-fixation. The samples were dehydrated in a graded ethanol series and then embedded in Quetol 812. Areas containing cells with aggregate morphology were block-mounted and cut into 90-nm sections. The sections were counterstained with uranyl acetate and lead citrate, and then examined with an H-7100 electron microscope.

Analysis of inclusion bodies (light microscopy and electron microscopy)

Sections of SK-N-SH cells containing eosinophilic hyaline inclusion bodies and spinal cord sections from transgenic SOD1 L84V mice were decolorized, rehydrated, rinsed in 0.1 M PBS, and then blocked for 1 h in 0.1 M PBS containing 0.3% Triton X-100 and 3% BSA. Next, the sections were incubated overnight at 4°C with the primary antibody (polyclonal sheep anti-SOD1 antibody at 1:500) in 0.1 M PBS containing 0.3% Triton X-100 and 3% BSA. After washing in 0.1 M PBS, sections were incubated for 30 min with the secondary antibody (biotinylated anti-sheep IgG). Subsequently, incubation was performed for 30 min in 3% H_2O_2 to eliminate endogenous peroxidases. After amplification with avidin-biotin complex (ABC kit, Vector Laboratories), visualization of reaction products was done with 0.05 M TBS (pH 7.6) containing 1.25% DAB and 0.75% hydrogen peroxide.

For electron microscopy, samples of SK-N-SH cells expressing L84V SOD1 and spinal cords from transgenic SOD1 L84V mice were decolorized, rehydrated, and rinsed in 0.1 M PBS. The samples were further fixed and dehydrated. Then the samples were embedded directly in epoxy resin, sectioned, counterstained, and examined as described under electron microscopy section.

SUPPORTING INFORMATION

Figure S1 Cytosolic localization of SOD1 in wt SOD1 expressing cells under ER stress. (A-F, A′-F′) Analysis of localization of SOD1 on ER. WT SOD1-expressing SK-N-SH cells were incubated for 24 h without (A-F) or with 1 ug/ml of tunicamycin (A′-F′). Then the cells were fixed and stained using an anti-SOD1 antibody (green; A, D, A′, D′) and an anti-KDEL antibody (red; B, B′) or an anti-GRP78 antibody (red; E, E′). GFP-cytochrome b5 were transfected to the cells and stained with anti-GFP (green; G, G′) and anti-SOD1 (red; H, H′) antibodies. Merged images (C, F, I, C′ F′, I′). (J-R, J′-R′) Analysis of SOD1 localization to the mitochondria. WT SOD1-expressing SK-N-SH cells were treated as described in above. The locations of the mitochondria and SOD1 were visualized in WT SOD1-expressing SK-N-SH cells using 100 nM Mito-tracker (red; K, K′), an anti-Tim17 antibody (red; N, N′) or an anti-Tom20 antibody (red; Q, Q′) and an anti-SOD1 antibody (green; J, M, P, J′, M′, P′). Merged images (L, O, R, L′, O′, R′). (S-U, S′-U′) Investigation of SOD1 localization to the Golgi apparatus. L84V SOD1-expressing SK-N-SH cells were treated as described in above. Then the cells were stained with anti-SOD1 antibody (green; S, S′) and anti-GM130 antibody (red; T, T′). Merged images (U, U′). (V-X, V′-X′) Analysis of the localization of SOD1 to the lysosomes. A GFP-tagged WT SOD1 vector was transfected into WT SOD1-expressing SK-N-SH cells. After 24 h of incubation with 1 ug/ml of tunicamycin, the cells were incubated for a further 30 min with 100 nM Lyso-tracker (red; W, W′) to visualize the lysosomes. GFP channel (V, V′) Merged images (X, X′). Scale bars = 20 um.
Found at: doi:10.1371/journal.pone.0001030.s001 (3.70 MB TIF)

ACKNOWLEDGMENTS

We are grateful to Dr. Otera and Prof. Mihara (Kyusyu University, Graduate School of Medical Science) and Dr. J. Niwa and Prof. G. Sobue (Nagoya University, Graduate School of Medicine) for providing anti-Tim17 and anti-Tom20 antibodies and myc-tagged ubiquitin expression vector, respectively. We thank Dr. K. Oono, Dr. S. Matsuda and Dr. T. Kudo (Osaka University, Graduate School of Medicine) for discussion and valuable advice. We thank Dr. George Wilkinson (Max-Planck Institute of Neurobiology) for critically reading the manuscript.

Author Contributions

Conceived and designed the experiments: SY YK TK SK MT. Performed the experiments: SY YK TK MT. Analyzed the data: SY YK TK MT JH MK MA YI SK MT. Contributed reagents/materials/analysis tools: SY YK TK MK MA YI. Wrote the paper: SY YK TK SK MT.

REFERENCES

1. Gurney ME (2000) What transgenic mice tell us about neurodegenerative disease. Bioessays 22: 297–304.
2. Brown RH Jr., Robberecht W (2001) Amyotrophic lateral sclerosis: pathogenesis. Semin Neurol 21: 131–139.
3. Cleveland DW, Rothstein JD (2001) From Charcot to Lou Gehrig: deciphering selective motor neuron death in ALS. Nat Rev Neurosci 2: 806–819.
4. Rowland LP, Shneider NA (2001) Amyotrophic lateral sclerosis. N Engl J Med 344: 1688–1700.
5. Julien JP (2001) Amyotrophic lateral sclerosis. unfolding the toxicity of the misfolded. Cell 104: 581–591.
6. Bruijn LI, Miller TM, Cleveland DW (2004) Unraveling the mechanisms involved in motor neuron degeneration in ALS. Annu Rev Neurosci 27: 723–749.
7. Rosen DR, Siddique T, Patterson D, Figlewicz DA, Sapp P, et al. (1993) Mutations in Cu/Zn superoxide dismutase gene are associated with familial amyotrophic lateral sclerosis. Nature 362: 59–62.
8. Forman MS, Lee VM, Trojanowski JQ (2003) 'Unfolding' pathways in neurodegenerative disease. Trends Neurosci 26: 407–410.
9. Kaufman RJ (2002) Orchestrating the unfolded protein response in health and disease. J Clin Invest 110: 1389–1398.
10. Tirasophon W, Welihinda AA, Kaufman RJ (1998) A stress response pathway from the endoplasmic reticulum to the nucleus requires a novel bifunctional protein kinase/endoribonuclease (Ire1p) in mammalian cells. Genes Dev 12: 1812–1824.
11. Wang B, Nguyen M, Breckenridge DG, Stojanovic M, Clemons PA, et al. (2003) Uncleaved BAP31 in association with A4 protein at the endoplasmic reticulum is an inhibitor of Fas-initiated release of cytochrome c from mitochondria. J Biol Chem 278: 14461–14468.
12. Bonifacino JS, Weissman AM (1998) Ubiquitin and the control of protein fate in the secretory and endocytic pathways. Annu Rev Cell Dev Biol 14: 19–57.
13. Travers KJ, Patil CK, Wodicka L, Lockhart DJ, Weissman JS, et al. (2000) Functional and genomic analyses reveal an essential coordination between the unfolded protein response and ER-associated degradation. Cell 101: 249–258.
14. Urano F, Wang X, Bertolotti A, Zhang Y, Chung P, et al. (2000) Coupling of stress in the ER to activation of JNK protein kinases by transmembrane protein kinase IRE1. Science 287: 664–666.
15. Nakagawa T, Yuan J (2000) Cross-talk between two cysteine protease families. Activation of caspase-12 by calpain in apoptosis. J Cell Biol 150: 887–894.
16. Nakagawa T, Zhu H, Morishima N, Li E, Xu J, et al. (2000) Caspase-12 mediates endoplasmic-reticulum-specific apoptosis and cytotoxicity by amyloid-beta. Nature 403: 98–103.
17. Katayama T, Imaizumi K, Sato N, Miyoshi K, Kudo T, et al. (1999) Presenilin-1 mutations downregulate the signalling pathway of the unfolded-protein response. Nat Cell Biol 1: 479–485.
18. Katayama T, Imaizumi K, Honda A, Yoneda T, Kudo T, et al. (2001) Disturbed activation of endoplasmic reticulum stress transducers by familial Alzheimer's disease-linked presenilin-1 mutations. J Biol Chem 276: 43446–43454.

19. Dickson KM, Bergeron JJ, Shames I, Colby J, Nguyen DT, et al. (2002) Association of calnexin with mutant peripheral myelin protein-22 ex vivo: a basis for "gain-of-function" ER diseases. Proc Natl Acad Sci U S A 99: 9852–9857.
20. Nishitoh H, Matsuzawa A, Tobiume K, Saegusa K, Takeda K, et al. (2002) ASK1 is essential for endoplasmic reticulum stress-induced neuronal cell death triggered by expanded polyglutamine repeats. Genes Dev 16: 1345–1355.
21. Takahashi R, Imai Y (2003) Pael receptor, endoplasmic reticulum stress, and Parkinson's disease. J Neurol 250 Suppl 3: III25–29.
22. Takahashi R, Imai Y, Hattori N, Mizuno Y (2003) Parkin and endoplasmic reticulum stress. Ann N Y Acad Sci 991: 101–106.
23. Hitomi J, Katayama T, Eguchi Y, Kudo T, Taniguchi M, et al. (2004) Involvement of caspase-4 in endoplasmic reticulum stress-induced apoptosis and Abeta-induced cell death. J Cell Biol 165: 347–356.
24. Kato S, Takikawa M, Nakashima K, Hirano A, Cleveland DW, et al. (2000) New consensus research on neuropathological aspects of familial amyotrophic lateral sclerosis with superoxide dismutase 1 (SOD1) gene mutations: inclusions containing SOD1 in neurons and astrocytes. Amyotroph Lateral Scler Other Motor Neuron Disord 1: 163–184.
25. Kato S, Horiuchi S, Liu J, Cleveland DW, Shibata N, et al. (2000) Advanced glycation endproduct-modified superoxide dismutase-1 (SOD1)-positive inclusions are common to familial amyotrophic lateral sclerosis patients with SOD1 gene mutations and transgenic mice expressing human SOD1 with a G85R mutation. Acta Neuropathol (Berl) 100: 490–505.
26. Kato S, Saito M, Hirano A, Ohama E (1999) Recent advances in research on neuropathological aspects of familial amyotrophic lateral sclerosis with superoxide dismutase 1 gene mutations: neuronal Lewy body-like hyaline inclusions and astrocytic hyaline inclusions. Histol Histopathol 14: 973–989.
27. Hirano A, Kurland LT, Sayre GP (1967) Familial amyotrophic lateral sclerosis. A subgroup characterized by posterior and spinocerebellar tract involvement and hyaline inclusions in the anterior horn cells. Arch Neurol 16: 232–243.
28. Wate R, Ito H, Zhang JH, Ohnishi S, Nakano S, et al. (2005) Expression of an endoplasmic reticulum-resident chaperone, glucose-regulated stress protein 78, in the spinal cord of a mouse model of amyotrophic lateral sclerosis. Acta Neuropathol (Berl) 110: 557–562.
29. Aoki M, Abe K, Houi K, Ogasawara M, Matsubara Y, et al. (1995) Variance of age at onset in a Japanese family with amyotrophic lateral sclerosis associated with a novel Cu/Zn superoxide dismutase mutation. Ann Neurol 37: 676–679.
30. Shibata N, Hirano A, Kobayashi M, Siddique T, Deng HX, et al. (1996) Intense superoxide dismutase-1 immunoreactivity in intracytoplasmic hyaline inclusions of familial amyotrophic lateral sclerosis with posterior column involvement. J Neuropathol Exp Neurol 55: 481–490.
31. Bruijn LI, Becher MW, Lee MK, Anderson KL, Jenkins NA, et al. (1997) ALS-linked SOD1 mutant G85R mediates damage to astrocytes and promotes rapidly progressive disease with SOD1-containing inclusions. Neuron 18: 327–338.
32. Niwa J, Ishigaki S, Hishikawa N, Yamamoto M, Doyu M, et al. (2002) Dorfin ubiquitylates mutant SOD1 and prevents mutant SOD1-mediated neurotoxicity. J Biol Chem 277: 36793–36798.
33. Urushitani M, Kurisu J, Tateno M, Hatakeyama S, Nakayama K, et al. (2004) CHIP promotes proteasomal degradation of familial ALS-linked mutant SOD1 by ubiquitinating Hsp/Hsc70. J Neurochem 90: 231–244.
34. Higgins CM, Jung C, Ding H, Xu Z (2002) Mutant Cu, Zn superoxide dismutase that causes motoneuron degeneration is present in mitochondria in the CNS. J Neurosci 22: RC215.
35. Tobisawa S, Hozumi Y, Arawaka S, Koyama S, Wada M, et al. (2003) Mutant SOD1 linked to familial amyotrophic lateral sclerosis, but not wild-type SOD1, induces ER stress in COS7 cells and transgenic mice. Biochem Biophys Res Commun 303: 496–503.
36. Kikuchi H, Almer G, Yamashita S, Guegan C, Nagai M, et al. (2006) Spinal cord endoplasmic reticulum stress associated with a microsomal accumulation of mutant superoxide dismutase-1 in an ALS model. Proc Natl Acad Sci U S A 103: 6025–6030.
37. Sasaki S, Warita H, Abe K, Iwata M (2005) Impairment of axonal transport in the axon hillock and the initial segment of anterior horn neurons in transgenic mice with a G93A mutant SOD1 gene. Acta Neuropathol (Berl) 110: 48–56.
38. Kato S, Nakashima K, Horiuchi S, Nagai R, Cleveland DW, et al. (2001) Formation of advanced glycation end-product-modified superoxide dismutase-1 (SOD1) is one of the mechanisms responsible for inclusions common to familial amyotrophic lateral sclerosis patients with SOD1 gene mutation, and transgenic mice expressing human SOD1 gene mutation. Neuropathology 21: 67–81.
39. Taylor JP, Hardy J, Fischbeck KH (2002) Toxic proteins in neurodegenerative disease. Science 296: 1991–1995.
40. Hyun DH, Lee M, Halliwell B, Jenner P (2003) Proteasomal inhibition causes the formation of protein aggregates containing a wide range of proteins, including nitrated proteins. J Neurochem 86: 363–373.
41. Kato S, Horiuchi S, Nakashima K, Hirano A, Shibata N, et al. (1999) Astrocytic hyaline inclusions contain advanced glycation endproducts in familial amyotrophic lateral sclerosis with superoxide dismutase 1 gene mutation: immunohistochemical and immunoelectron microscopical analyses. Acta Neuropathol (Berl) 97: 260–266.
42. Kato S, Sumi-Akamaru H, Fujimura H, Sakoda S, Kato M, et al. (2001) Copper chaperone for superoxide dismutase co-aggregates with superoxide dismutase 1 (SOD1) in neuronal Lewy body-like hyaline inclusions: an immunohistochemical study on familial amyotrophic lateral sclerosis with SOD1 gene mutation. Acta Neuropathol (Berl) 102: 233–238.
43. Kato S, Saeki Y, Aoki M, Nagai M, Ishigaki A, et al. (2004) Histological evidence of redox system breakdown caused by superoxide dismutase 1 (SOD1) aggregation is common to SOD1-mutated motor neurons in humans and animal models. Acta Neuropathol (Berl) 107: 149–158.
44. Bassik MC, Scorrano L, Oakes SA, Pozzan T, Korsmeyer SJ (2004) Phosphorylation of BCL-2 regulates ER Ca(2+) homeostasis and apoptosis. Embo J 23: 1207–1216.
45. Wootz H, Hansson I, Korhonen L, Lindholm D (2006) XIAP decreases caspase-12 cleavage and calpain activity in spinal cord of ALS transgenic mice. Exp Cell Res 312: 1890–1898.
46. Wootz H, Hansson I, Korhonen L, Napankangas U, Lindholm D (2004) Caspase-12 cleavage and increased oxidative stress during motoneuron degeneration in transgenic mouse model of ALS. Biochem Biophys Res Commun 322: 281–286.
47. Ishihara N, Mihara K (1998) Identification of the protein import components of the rat mitochondrial inner membrane, rTIM17, rTIM23, and rTIM44. J Biochem (Tokyo) 123: 722–732.
48. Kanaji S, Iwahashi J, Kida Y, Sakaguchi M, Mihara K (2000) Characterization of the signal that directs Tom20 to the mitochondrial outer membrane. J Cell Biol 151: 277–288.
49. Kato H, Sakaki K, Mihara K (2006) Ubiquitin-proteasome-dependent degradation of mammalian ER stearoyl-CoA desaturase. J Cell Sci 119: 2342–2353.

Journal of Neuroscience Research 85:2332–2342 (2007)

Hepatocyte Growth Factor Promotes Endogenous Repair and Functional Recovery After Spinal Cord Injury

Kazuya Kitamura,[1,2] Akio Iwanami,[1–3] Masaya Nakamura,[1] Junichi Yamane,[1,2] Kota Watanabe,[1] Yoshinori Suzuki,[4] Daisuke Miyazawa,[4] Shinsuke Shibata,[2] Hiroshi Funakoshi,[4] Shinichi Miyatake,[5] Robert S. Coffin,[6] Toshikazu Nakamura,[4] Yoshiaki Toyama,[1] and Hideyuki Okano[2]*

[1]Department of Orthopaedic Surgery, Keio University School of Medicine, Shinjuku, Tokyo, Japan
[2]Department of Physiology, Keio University School of Medicine, Shinjuku, Tokyo, Japan
[3]Clinical Research Center, National Hospital Organization, Murayama Medical Center, Musashimurayama, Tokyo, Japan
[4]Division of Molecular Regenerative Medicine, Osaka University Graduate School of Medicine, Suita, Osaka, Japan
[5]Department of Neurosurgery, Osaka Medical College, Takatsuki, Osaka, Japan
[6]Department of Molecular Pathology, Windeyer Institute of Medical Science of University College, London, United Kingdom

Many therapeutic interventions using neurotrophic factors or pharmacological agents have focused on secondary degeneration after spinal cord injury (SCI) to reduce damaged areas and promote axonal regeneration and functional recovery. Hepatocyte growth factor (HGF), which was identified as a potent mitogen for mature hepatocytes and a mediator of inflammatory responses to tissue injury, has recently been highlighted as a potent neurotrophic and angiogenic factor in the central nervous system (CNS). In the present study, we revealed that the extent of endogenous HGF up-regulation was less than that of c-Met, an HGF receptor, during the acute phase of SCI and administered exogenous HGF into injured spinal cord using a replication-incompetent herpes simplex virous-1 (HSV-1) vector to determine whether HGF exerts beneficial effects and promotes functional recovery after SCI. This treatment resulted in the significant promotion of neuron and oligodendrocyte survival, angiogenesis, axonal regrowth, and functional recovery after SCI. These results suggest that HGF gene delivery to the injured spinal cord exerts multiple beneficial effects and enhances endogenous repair after SCI. This is the first study to demonstrate the efficacy of HGF for SCI.

Key words: hepatocyte growth factor; spinal cord injury; repair; functional recovery

Spinal cord injury (SCI) is followed by secondary degeneration, which is characterized by progressive tissue necrosis, and many experimental interventions using neurotrophic factors have focused on this posttraumatic inflammatory process to reduce damaged area and promote axonal regeneration throughout the lesion epicenter. Neurotrophins such as nerve growth factor (NGF; Tuszynski et al., 1994, 1996), brain-derived growth factor (BDNF; Jakeman et al., 1998; Vavrek et al., 2006), neurotrophin-3 (NT-3; Grill et al., 1997; McTigue et al., 1998), and glial cell line-derived neurotrophic factor (GDNF; Liu et al., 1999; Blesch and Tuszynski, 2001) have been reported to enhance axonal growth in injured spinal cord, and some of the studies cited above showed that neurotrophins promoted behavioral recovery after SCI (Jakeman et al., 1998; Liu et al., 1999).

Not only neurotrophic support but also angiogenesis after SCI is a critical factor in the endogenous regenerative response to trauma (Casella et al., 2002; Loy et al., 2002). Initial damage to local blood vessels is decisive for the progression of destructive events during secondary degeneration (Mautes et al., 2000) and strategic treatments to improve angiogenesis after SCI showed a relationship between blood flow and functional recovery (Glaser et al., 2004; Guizar-Sahagun et al., 2005). Hepatocyte growth

The first two authors contributed equally to this work.

Contract grant sponsor: Leading Project for the Realization of Regenerative Medicine from the Ministry of Education, Culture, Sports, Science and Technology (MEXT), Japan; Contract grant sponsor: General Insurance Association of Japan; Contract grant sponsor: Terumo Foundation Life Science Foundation (to H.O.); Contract grant sponsor: Grant-in-Aid for the 21st Century COE Program from MEXT (to Keio University); Contract grant sponsor: Keio Gijuku Academic Development Funds.

*Correspondence to: Hideyuki Okano, 35 Shinanomachi, Shinjuku-ku, Tokyo 160-8582, Japan. E-mail: hidokano@sc.itc.keio.ac.jp

Received 1 March 2007; Accepted 26 March 2007

Published online 4 June 2007 in Wiley InterScience (www.interscience.wiley.com). DOI: 10.1002/jnr.21372

factor (HGF) was first identified as a potent mitogen for mature hepatocytes (Nakamura et al., 1984; Nakamura et al., 1989) and a natural ligand for the c-Met protooncogene product (Bottaro et al., 1991). Recent studies have revealed that HGF acts as a neurotrophic factor in a variety type of neurons (Hamanoue et al., 1996; Maina and Klein, 1999; Caton et al., 2000) and that HGF administration enhances angiogenesis, improves microcirculation, inhibits the destruction of the blood–brain barrier (Date et al., 2004), and exerts a neurotroprotective effects after cereberal ischemia (Miyazawa et al., 1998; Shimamura et al., 2006). In the present study, we first examined the changes in endogenous HGF and c-Met expression after rat SCI and then determined whether the administration of exogenous HGF into the injured spinal cord using HSV-1 vector had positive effects on histological changes and the motor function after SCI. To the best of our knowledge, this is the first study to examine the efficacy of HGF for SCI.

MATERIALS AND METHODS

Administration of HGF by HSV-1 Vector and SCI

Adult female Sprague-Dawley rats (230–250 g; Clea, Tokyo, Japan) were used for all the experimental groups. All animals were handled in accordance with the Laboratory Animal Welfare Act, the *Guide for the care and use of laboratory animals* (National Institutes of Health), and the guidelines and policies for animal surgery provided by the Animal Study Committee of the Central Institute for Experimental Animals of Keio University. Rreplication-incompetent HSV-1 vectors, HSV-HGF and HSV-LacZ, were obtained as described by Zhao et al. (2006). Rats were anesthetized, their spinal cords were exposed by laminectomy at T10, and 10 μl of HSV-HGF or HSV-LacZ (each titer 1.3×10^9 pfu/ml) was injected into the spinal cord in the HGF group or the LacZ group, respectively ($n = 62$ each). At 3 days after HSV-1 vector injection, the spinal cords were again exposed at the site of injection, and the region was contused by using the Infinite Horizon impactor (200 kdyn; Precision Systems, Lexington, KY). In the SCI group, contusive SCI was induced at T10 using the IH impactor without the prior injection of HSV-1 vectors ($n = 75$).

Enzyme-Linked Immunosorbent Assay

Plasma samples were withdrawn transcardially, and a 4-mm-long segment of spinal cord at T10 was isolated and lysed at the indicated times. The spinal cord lysates were prepared with 50 mM Tris-HCl (pH 7.4), 2 M NaCl, 25 mM β-glycerophosphate, 25 mM NaF, 1% Triton X-100, 1 mM phenylmethylsulfonylfluoride (PMSF; Wako, Osaka, Japan), 2 mg/ml antipain (Peptide Institute Inc., Osaka, Japan), 2 mg/ml leupeptin (Peptide Institute Inc.), and 2 mg/ml pepstatin (Peptide Institute Inc.). The concentrations of HGF protein in the extracts of spinal cords lysates and plasma were determined by using ELISA kits (Institute of Immunology, Tokyo, Japan).

Real-Time Quantitative RT-PCR

A 4-mm-long spinal cord segment at T10 was collected at indicated times, and total RNA was isolated from each spinal cord sample using an RNeasy Kit (Qiagen, Bethesda, MD). The levels of HGF and c-Met mRNA were measured as previously described (Sun et al., 2000). The quantitative data for each sample at indicated times was used to determine the ratio relative to that in intact spinal cord.

Immunoblotting Analysis

Lysates from each 4-mm-long spinal cord at T10 were prepared in the same buffer used in an ELISA at indicated times. Proteins (20 μg) were resolved via SDS-PAGE, transferred to a polyvinylidene difluoride membrane, and immunoblotted with a polyclonal antibody (anticleaved caspase-3; 1:500; Cell Signaling Technology, Beverly, MA). Bands were visualized by using an ECL Blotting Analysis System (Amersham Bioscience, Arlington Heights, IL), and the band intensities were measured with an NIH image analyzer. The quantitative data for each band show the relative ratio to that of the spinal cord lysate at 3 days after SCI without any HSV-1 vector injection.

Immunohistochemistry

Spinal cords were perfusion fixed with 4% paraformaldehyde in 0.1 M phosphate-buffered saline (PBS) and postfixed in the same fixative (24 hr), 10% sucrose in 0.1 M PBS (24 hr), and 30% sucrose in 0.1 M PBS (24 hr). Segments of spinal cords were embedded in optimal cutting temperature compound and cut on a cryostat into 20-μm-thick sections. For immunofluoroscence staining, the sections were incubated at 4°C with monoclonal anti-NeuN (1:200; Chemicon, Temecula, CA), monoclonal antiglial fibrillary acidic protein (GFAP; 1:500; Sigma, St. Louis, MO), monoclonal anti-GST-π (1:500; BD Bioscience Pharmingen, San Diego, CA), and polyclonal anti-c-Met (1:50; Santa Cruz Biotechnology, Santa Cruz, CA), followed by Alexa Fluoro-conjugated secondary antibodies (1:500; Molecular Probes, Eugene, OR) and polyclonal anti-rat HGF (1:1; Institute of Immunology) and polyclonal anticleaved caspase-3 (1:400; Cell Signaling), followed by biotinylated secondary antibodies (1:500; Jackson Immunoresearch, West Groove, PA). For diaminobenzidine staining, the sections were incubated at 4°C with polyclonal anti-5-hydroxytryptamine (5-HT; 1:100; Dia Sorin, Stillwater, MN), polyclonal anticholine acetyltransferase (ChAT; 1:50; Chemicon), monoclonal anti-rat endothelial cell antigen-1 (RECA-1; 1:25; Serotec, Raleigh, NC), monoclonal anti-growth-associated protein-43 (GAP-43; 1:2,000; Chemicon), and monoclonal antineurofilament 200 kD (RT97; 1:2,000; Chemicon), followed by biotinylated secondary antibodies (1:500; Jackson Immunoresearch). Biotinylated antibodies were visualized using the Vectastain Elite ABC kit (Vector Laboratories, Burlingame, CA), followed by TSA (Vector Laboratories) or diaminobenzidine (Sigma). All the images were obtained via microscopy (Axioskop 2 Plus; Zeiss, Oberkochen, Germany) or confocal microscopy (LSM510; Zeiss).

Quantitative Analyses

To quantify the RECA-1-positive area and Luxol fast blue (LFB)-stained myelinated area, the images of axial sections were obtained. To quantify the area of the GAP-43-positive fibers and the RT97-positive fibers, the midsagittal sections were scanned and tiled transversely throughout a cephalocaudal

length of 175 μm at the indicated levels of injured spinal cords with a CCD camera (DXC-390; Sony, Tokyo, Japan) using a Micro Computer Imaging Device (MCID; Imaging Research Inc., St. Catharines, Ontario, Canada). The obtained images were analyzed using grain counting with the light intensity by MCID. Threshold values were maintained at constant levels for all analyses. Images of axial sections stained with hematoxylin and eosin were obtained, and manually outlined areas of cavitation were also quantified by MCID. Images of axial sections stained with anti-ChAT antibody and anti-RECA-1 antibody were obtained, and the numbers of ChAT-positive motoneurons in the ventral horns and the numbers of RECA-1-positive vessels with lumina larger than 20 μm were counted.

Behavioral Testing

Motor function of the hindlimbs was evaluated by open-field testing using the methodology of the Basso-Beattie-Bresnahan (BBB) scale at 4, 7, 14, 21, 28, 35, and 42 days after SCI (n = 14 for each group). Throughout the surgery, behavioral testing, and histological analyses, the three researchers who performed the procedures were unaware of the groups to which the rats belonged.

Statistical Analysis

All data are reported as the mean ± SEM. An unpaired two-tailed Student's *t*-test was used for single comparisons. The results of the real-time PCR and ELISA experiments were analyzed via Dunnett test. The Mann-Whitney U-test was used for the BBB score.

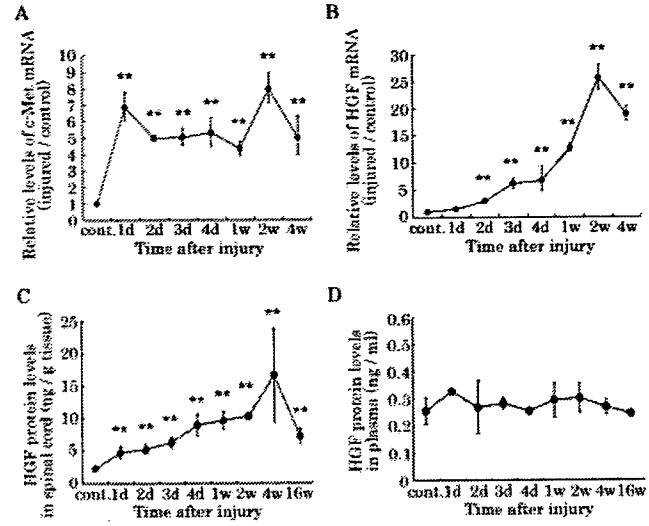

Fig. 1. Endogenous regulation of HGF and c-Met expression after SCI. The levels of c-Met mRNA and HGF mRNA expression after SCI in a 4-mm segment of spinal cord from the lesion epicenter were analyzed by using real-time RT-PCR. In contrast to a drastic increase in c-Met mRNA expression during the acute phase of SCI (**A**), HGF mRNA expression showed a gradual increase only during the subacute phase (**B**). ELISA data show that the amount of HGF protein in a 4-mm segment of spinal cord from the lesion epicenter gradually increased during the subacute phase of SCI (**C**), similar to the pattern of HGF mRNA expression, and the plasma HGF levels did not increase significantly after SCI (**D**). All data were reported as the mean ± SEM. $^{**}P < 0.01$; n > 3 each.

RESULTS

Endogenous Up-Regulation of HGF in Injured Spinal Cord Was Insufficient Compared With the Sharp Increase of c-Met Expression During the Acute Phase of SCI

To determine the dynamics of the HGF-c-Met system in adult rat spinal cord after SCI, the levels of HGF and c-Met mRNA expression in injured spinal cord were analyzed via real-time RT-PCR, and the amounts of HGF protein in injured spinal cord and plasma were also analyzed by an ELISA in the SCI group. Whereas the level of c-Met mRNA expression in injured spinal cord drastically increased from 1 day after SCI (Fig. 1A), the level of HGF mRNA expression gradually increased and peaked at 2 weeks after SCI (Fig. 1B). Thus HGF and c-Met mRNA expression peaked at different time points after SCI. Consistently with the level of HGF mRNA expression, the amount of HGF protein in injured spinal cord gradually increased, peaking at about 4 weeks after SCI (Fig. 1C). In contrast, the amount of HGF protein in the plasma did not increase after SCI (Fig. 1D). Next, we examined the localization of c-Met in normal and injured rat spinal cord. In intact thoracic spinal cord, c-Met immunoreactivity (c-Met-IR) was detected in NeuN-positive neurons and GST-π-positive oligodendrocytes, but not in astrocytes (Fig. 2A–I). However, at 1 week after SCI, c-Met-IR was clearly observed in GFAP-positive reactive astrocytes (Fig. 2J–L; axial section at 5 mm rostral to the epicenter) as well as in neurons and oligodendrocytes (data not shown).

To examine the distribution and amount of HGF protein in uninjured spinal cord after gene delivery, the spinal cord tissues were harvested and processed for an ELISA and HGF immunostaining at 3 days and 4 weeks after the HSV-1 vectors (HSV-HGF and HSV-LacZ) injection. Although HGF-IR showed a remarkable expansion putatively in the extracellular matrix in the HGF group at 3 days after injection, very little HGF-IR was observed in the LacZ group (Fig. 3A). Injection of the HSV-1 vectors resulted in a significantly higher amount of HGF protein in the HGF group (11.5 ± 0.8 ng/g tissue) compared with that in the LacZ group (3.4 ± 0.1 ng/g tissue) at 3 days after injection (Fig. 3C). Double immunostaining using anti-β-galactosidase antibody showed that LacZ gene expression was maintained in NeuN-positive neurons until 4 weeks after the injection (Fig. 3B). There was no significant difference in the amount of HGF protein between the HGF group (4.9 ± 1.5 ng/g tissue) and the LacZ group (2.9 ± 0.1 ng/g tissue) at 4 weeks after the injection (Fig. 3C).

HGF Promotes Survival of Neurons and Oligodendrocytes After SCI

To determine the effects of HGF gene delivery on the injured spinal cord, we performed several quantita-

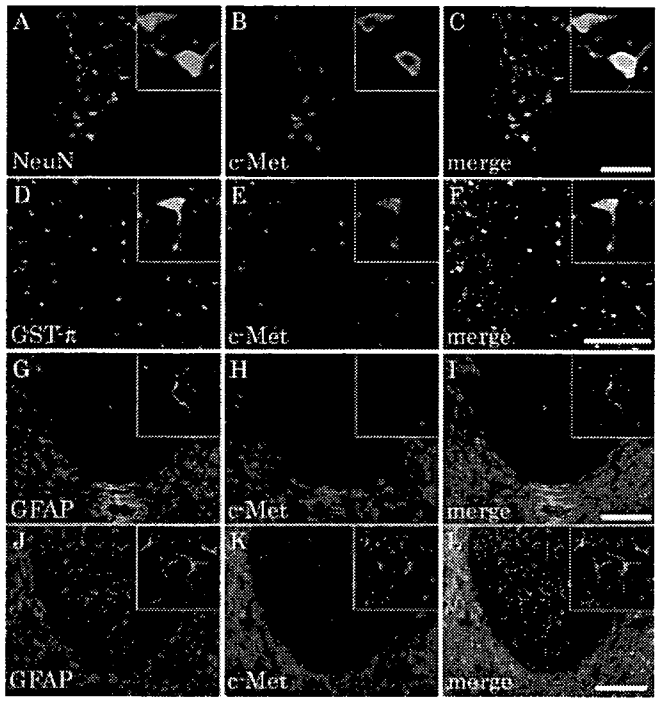

Fig. 2. Change in c-Met immunoreactivity (IR) in neurons, oligodendrocytes and astrocytes before and after SCI. Intact spinal cord showed c-Met-IR in NeuN-positive neurons (**A–C**) and GST-π-positive oligodendrocytes (**D–F**), but not in astrocytes (**G–I**). At 1 week after SCI, c-Met-IR was observed in GFAP-positive reactive astrocytes (**J–L**). **Insets** show magnified view. Scale bars = 200 μm in C (applies to A–C); 100 μm in F (applies to D–F); 200 μm in I (applies to G–I); 200 μm in L (applies to J–L).

tive histological analyses. First, the cavity area of the injured spinal cord at 6 weeks after SCI was obviously smaller in the HGF group than the LacZ group. Significant differences in the total cavity areas at the epicenter and at 4 mm rostral and caudal to the epicenter were observed between the two groups (Fig. 4A). Second, the HGF group obviously had more preserved myelinated areas than the LacZ group at 6 weeks after SCI. Notably, the HGF group exhibited a significantly spared rim of white matter, even at the lesion epicenter, whereas the LacZ group exhibited severely demyelinated white matter throughout the lesion epicenter. Quantitative analysis of the myelinated areas revealed significant differences between the two groups at all of the examined sites (Fig. 4B). Next, to determine the effect of HGF on motoneurons, the numbers of ChAT-positive motoneurons in the ventral horns were quantified at 6 weeks after SCI. Although almost all the ChAT-positive motoneurons had disappeared at the lesion epicenter in both groups, significantly larger numbers of ChAT-positive motoneurons were observed at the site rostral to the epicenter in the HGF group compared with that in the LacZ group (Fig. 4C). These findings suggested that HGF exerted protective effects on motoneurons and oligodendrocytes and contributed to tissue sparing after SCI.

Next, to determine whether HGF inhibited the activation of caspase-3 after SCI, immunoblotting analyses using anti-cleaved caspase-3 antibody were performed at 1, 3, and 7 days after SCI. Cleaved caspase-3 was strongly induced after SCI and was most detectable at 3 days after SCI in both the HGF and the LacZ groups (Fig. 5A). Quantitative analysis revealed that the induction of cleaved caspase-3 was significantly attenuated in the HGF group compared with the LacZ group at 3 days after SCI (Fig. 5B). Furthermore, double immunostaining with anti-cleaved caspase-3 antibody and antibodies for neurons or oligodendrocytes showed that the numbers of NeuN and cleaved caspase-3 double-positive motoneurons in the ventral horns and GST-π and cleaved caspase-3 double-positive oligodendrocytes were

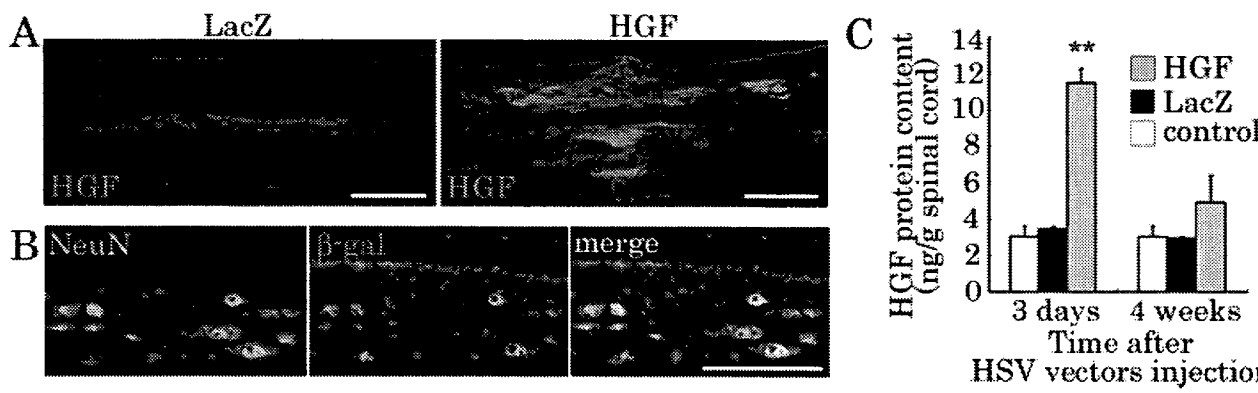

Fig. 3. Expression of exogenous HGF in the spinal cord introduced by HSV-HGF vector. Immunohistochemical staining of rat HGF in sagittal sections at 3 days after the HSV-1 vectors (HSV-HGF and HSV-LacZ) injection into the spinal cords showed remarkable HGF-IR in the extracellular matrix in the HGF group. In all the sagittal sections shown in the present study, the left side is the rostral side (**A**). β-Galactosidase expression was observed in neurons until 4 weeks after the HSV-LacZ injection (**B**). HGF protein levels in 4-mm segments of spinal cords at the site of the HSV-1 vectors injection were analyzed using an ELISA at 3 days and 4 weeks after the injection. The HGF group showed a significantly larger amount of HGF protein than in intact spinal cord (control) and the LacZ group at 3 days after injection. No significant difference in the amount of HGF protein was seen among the three groups at 4 weeks after the injection (**C**). $^{**}P < 0.01$; n = 3 each. Scale bars = 1 mm in A; 100 μm in B.

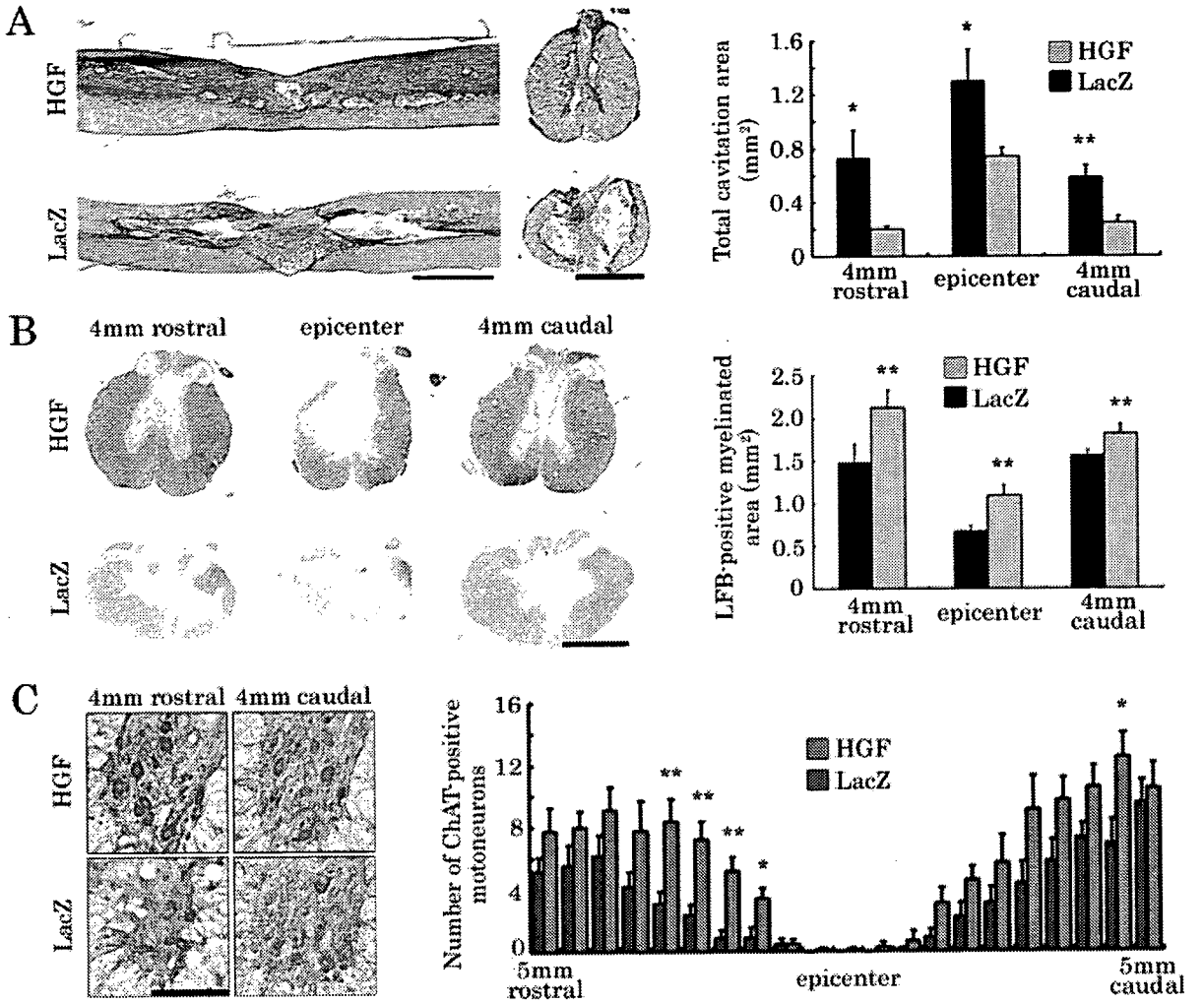

Fig. 4. Significant reduction in the size of damaged parenchyma in the HGF group. HE staining of midsagittal sections and the axial sections of lesion epicenter at 6 weeks after injury showed remarkably smaller areas of damage in the HGF group compared with the LacZ group. Significant differences in the total cavitation areas in the axial sections at the epicenter and at 4 mm rostral and caudal to the epicenter were observed between the two groups (n = 5 each; **A**). The axial sections stained with Luxol fast blue (LFB) at 6 weeks after injury showed a remarkable reduction in the area of demyelination in the HGF group compared with the LacZ group. Quantification of LFB-positive myelinated areas showed significant difference between the two groups at all of the examined sites (n = 5 each; **B**). The number of ChAT-positive motoneurons in the ventral horns at the lesion epicenter and adjacent sections up to 5 mm rostral and caudal to the epicenter in 0.5-mm increments was quantified at 6 weeks after SCI. The pictures show magnified views of right ventral horns of axial sections at 4 mm rostral and caudal to the epicenter. Significant differences between the two groups were observed mainly in the sections rostral to the epicenter (n = 5 each; **C**). $*P < 0.05$, $**P < 0.01$. Scale bars = 2 mm in A left; 1 mm in A right and B; 150 μm in C.

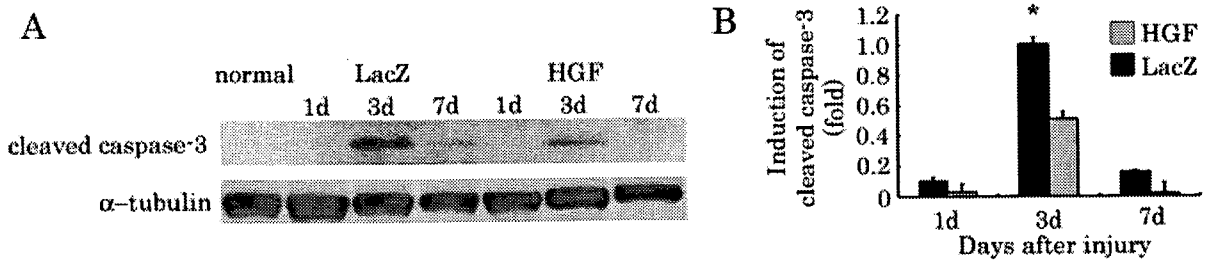

Fig. 5. Induction of cleaved caspase-3 in the injured spinal cord. Immunoblotting analyses showed remarkable induction of cleaved caspase-3 in the HGF and LacZ group during the acute phase of SCI, mainly at 3 days after SCI (**A**). Significantly attenuated cleaved caspase-3 induction was observed in the HGF group, compared with the LacZ group, at 3 days after SCI (n = 3 each; **B**). $*P < 0.05$.

obviously reduced in the HGF group compared with the LacZ group (data not shown). These results suggested that HGF significantly reduced the levels of cleaved caspase-3 activation in neurons and oligodendrocytes after SCI, thereby promoting their survival.

HGF Enhances Angiogenesis After SCI

To examine the effect of HGF on vascular endothelial cells after SCI, immunostaining with anti-RECA-1 antibody was performed. In intact thoracic spinal cord, the vessels had delicate walls composed of homogeneously stained endothelial cells. Although most of the vessels disappeared at the epicenter at 1 week after SCI, several vessels were stained intensely and showed abnormally large lumina with thick walls (Fig. 6A, arrows), which were not observed in the intact spinal cord. Quantitative MCID analysis of the RECA-1-positive areas showed significant differences at the epicenter and 4 mm rostral to the epicenter between the two groups (Fig. 6B). In these areas, there were large amounts of fragmented RECA-1-IR resulting from the debris of dead endothelial cells. Thus, we focused on RECA-1-positive vessels with intact lumina for quantitative analysis. Accordingly, we found that significant differences in the number of RECA-1-positive vessels with lumina larger than 20 μm, representing newly formed vessels (Casella et al., 2002), between the two groups at the epicenter and at 4 mm rostral to the epicenter at 1 week after SCI (Fig. 6C).

HGF Promotes Regrowth of Serotonergic Fibers and Functional Recovery After SCI

To determine the effects of HGF on the axonal growth after SCI, axial sections of injured spinal cords were immunostained with anti-5HT antibody at 1 week and 6 weeks after SCI. 5HT-positive raphe-spinal serotonergic fibers were observed mainly in the gray matter in each group. Quantitative MCID analyses revealed that, whereas 5HT-positive fibers were almost undetectable in either group at 1 week after SCI, a significantly greater abundance of 5HT-positive fibers was detected, even in an area 4 mm caudal to the epicenter, in the HGF group compared with that in the LacZ group (Fig. 7A, arrows) at 6 weeks after SCI (Fig. 7A,B). Furthermore, at 1 week after SCI, the 5HT-positive fibers also showed c-Met-IR (Fig. 7C), and, at 6 weeks after SCI, they expressed GAP-43, which has been used as a marker of axonal regeneration (Kobayashi et al., 1997; Ramon-Cueto et al., 1998; Ikegami et al., 2005; Kaneko et al., 2006), even in a region 4mm caudal to the epicenter (Fig. 7D). Consistently with this, a greater abundance of GAP-43-positive fibers (Fig. 7E,F) and RT97-positive fibers (Fig. 7G,H) was observed, even in a region 4 mm caudal to the epicenter, in the HGF group compared with the LacZ group at 6 weeks after SCI; furthermore, c-Met-IR was also detected in these fibers (Fig. 7I,J). Most of the RT97-positive fibers were oriented longitudinally and parallel to each other (Fig. 7G), and these longitudinal fibers did not express GAP-43 (data not shown), indicating that they probably represented preserved axons after SCI.

The contusive SCI resulted in complete paralysis, followed by gradual recovery, reaching a plateau (BBB score 6.6 ± 1.1) at 6 weeks after SCI in the LacZ group. In the HGF group also, the animals suffered complete paralysis at 1 day after SCI, but these animals eventually showed better functional recovery than those in the LacZ group. Significant differences in the BBB scores were observed between the two groups from 7 days after SCI (Fig. 8). We believe that the difference between a BBB score of 8 (sweeping of hindlimbs) and

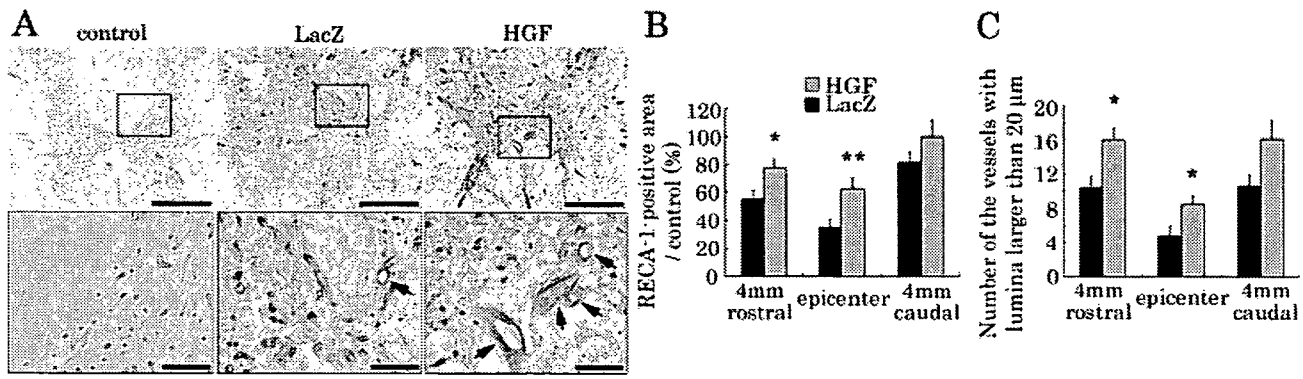

Fig. 6. Change in the microvasculature in the spinal cord after SCI. The axial sections of lesion epicenter at 1 week after SCI and intact thoracic spinal cord were immunostained with anti-RECA-1 antibody (**A**). Higher magnification views correspond to the boxed areas in the upper pictures. RECA-1-positive vessels with abnormally large lumina (arrows) emerged at 1 week after SCI in the two groups; these vessels were not observed in intact spinal cord and were considered to represent newly formed vessels after SCI. Quantitative analysis of the total area of RECA-1-positive endothelial cells (**B**) and the number of vessels with lumina larger than 20 μm (**C**) showed significant differences at the epicenter and at 4 mm rostral to the epicenter between the two groups. $*P < 0.05$, $**P < 0.01$; n = 5 each. Scale bars = 500 μm in A upper; 100 μm in A lower.

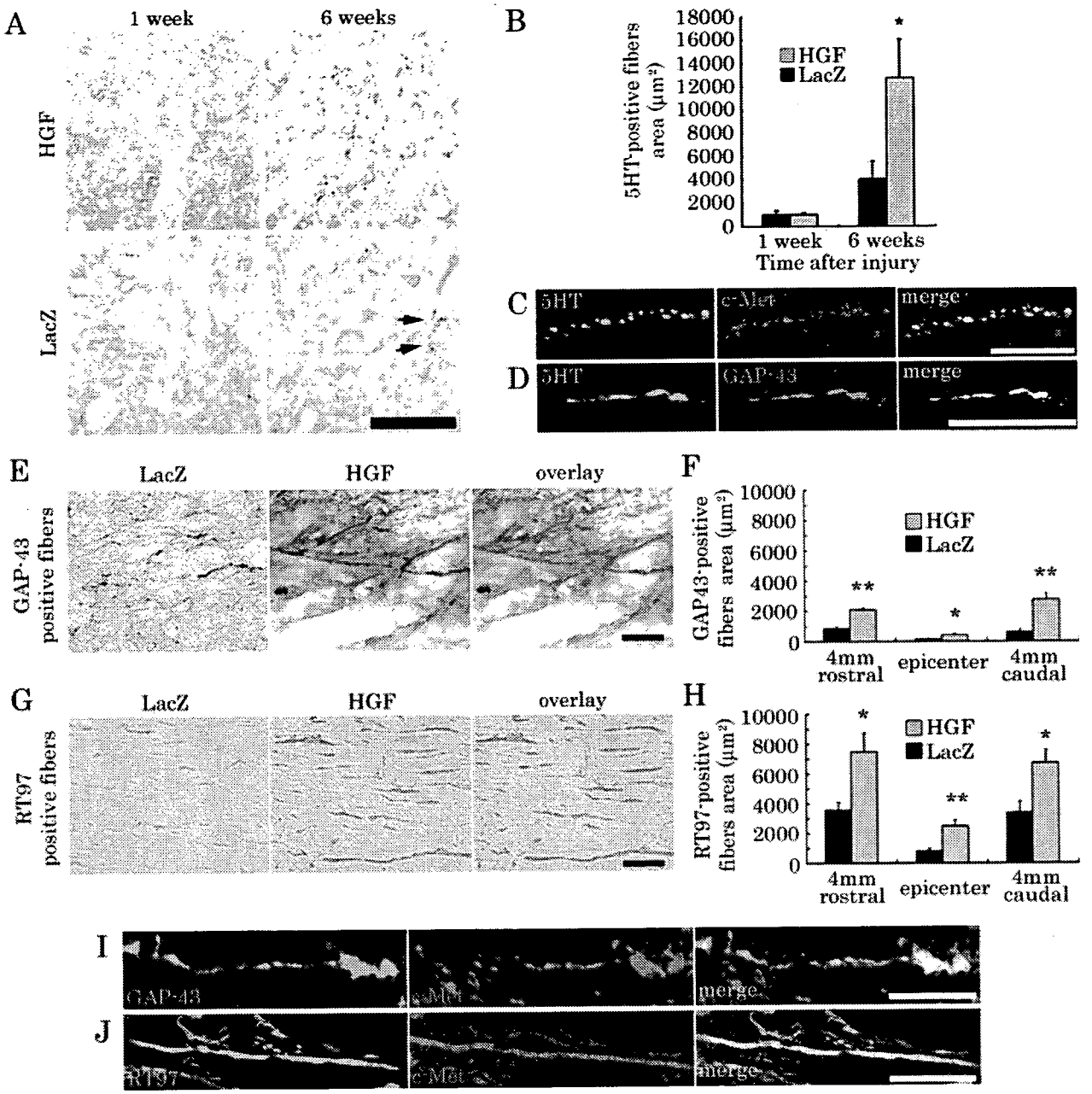

Fig. 7. Degeneration and regrowth of fibers after SCI. Immunostaining and quantification of 5-HT-positive fibers in axial sections at 4 mm caudal to the epicenter showed no significant difference between the two groups at 1 week after SCI but showed significant regrowth of the fibers in the HGF group compared with poor regrowth in the LacZ group (arrows) at 6 weeks after SCI (n = 5 each; **A,B**). 5HT-positive descending raphe-spinal fibers showed c-Met-IR (axial section) at 1 week after SCI (**C**) and expressed GAP-43 (sagittal section) at 4 mm caudal to the epicenter at 6 weeks after SCI (**D**). Representative images of midsagittal sections through an area 4 mm caudal to the epicenter showed a significantly greater abundance of GAP-43-positive fibers (**E**) and R97-positive fibers (**G**) in the HGF group compared with that in the LacZ group at 6 weeks after SCI. Note that significant differences in the immunopositive area were observed even in the region 4 mm caudal to the epicenter between the two groups (n = 5 each; **F,H**). Double immunostaining of midsagittal sections at 1 week after SCI showed c-Met-IR in the GAP-43-positive growth cones (**I**) and RT97-positive neurofilaments (**J**). $\star P < 0.05$, $\star\star P < 0.01$. Scale bars = 50 μm in A,E,G,J; 20 μm in C,D; 10 μm in I.

a BBB score of 9 (weight support on hindlimbs) is clinically substantial. From a clinical perspective, the recovery of the HGF group to weight-supported plantar steps (BBB score 10.1 ± 0.6) was noteworthy.

DISCUSSION

Previous studies have shown that the HGF-c-Met system is involved in the mediation of inflammatory responses to tissue injury. In animal models in which the

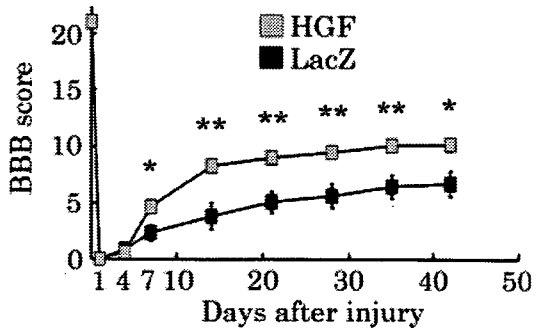

Fig. 8. BBB scores after SCI. A significant improvement in hindlimb motor function was observed in the HGF group compared with the LacZ group from 7 days after SCI (n = 14 each). $*P < 0.05$, $**P < 0.01$.

liver (Noji et al., 1990; Kono et al., 1992; Matsumoto and Nakamura, 1997), lung (Yanagita et al., 1993), or kidney (Kono et al., 1992; Igawa et al., 1993) tissues were experimentally damaged, the HGF mRNA expression and HGF activity were found to increase markedly in the damaged organs, peaking within 24 hr after the insult. Consistently with these increased expressions, the plasma HGF level also increased within 24 hr after the damage, suggesting that HGF could be delivered to these injured organs from other organs through the blood supply via an endocrine mechanism, in addition to being produced endogenously in these organs (Kono et al., 1992). In the CNS, on the other hand, it was reported that HGF mRNA was up-regulated exclusively in the periinfarct region at 14 days after cerebral ischemia (Nagayama et al., 2004). In the present study, we demonstrated for the first time that the HGF mRNA expression level gradually increased, peaking at 2 weeks after SCI, whereas the c-Met mRNA expression level increased markedly within 1 day of SCI. In addition, no increase in the plasma HGF levels was found after SCI. These findings suggest that the injured spinal cord cannot produce a sufficient amount of HGF by itself, compared with the remarkable increase in c-Met expression after SCI, nor can HGF be supplied through an endocrine mechanism, in contrast to the case following damage to other organs, as mentioned above. These results prompted us to perform an in vivo study to determine whether the application of exogenous HGF into the injured spinal cord might exert a beneficial effect and promote functional recovery in the spinal cord after SCI. We used the HSV-1 vector to introduce the exogenous HGF into the spinal cord, to compensate for the deficiency of endogenous HGF after SCI. The feasibility of using this vector for transgene expression in the nervous system in a safe and nontoxic manner has been examined in previous studies (Coffin et al., 1998; Palmer et al., 2000; Lilley et al., 2001).

We showed that the application of exogenous HGF into the injured spinal cord significantly attenuated caspase-3 activation in both neurons and oligodendrocytes, thereby reducing the area of demyelination and promoting the survival of cholinergic neurons. Previous studies have demonstrated the neurotrophic effects of HGF on a variety of neurons (Hamanoue et al., 1996; Maina and Klein, 1999; Caton et al., 2000), and, in one study, the application of HGF prevented the apoptosis of adult motoneurons after axonotomy of the hypoglossal nerve (Okura et al., 1999). In addition, HGF overexpression was reported to prevent delayed neuronal death and decrease the infarct volume after cerebral ischemia (Miyazawa et al., 1998; Hayashi et al., 2001; Shimamura et al., 2004; Niimura et al., 2006) by attenuating apoptosis. Consistently with these reports, in the present study, the neurotrophic and antiapoptotic effects of HGF on the neurons prevented neuronal loss after SCI, thereby reducing the size of the damaged area. Oligodendrocyte death, which is mediated by a pathway involving caspase-11 and caspase-3, leads to demyelination (Hisahara et al., 2001), and inhibition of the apoptosis of oligodendrocytes has been shown to reduce the area of demyelination and functional impairment after SCI (Tamura et al., 2005). These reports indicate that the induction of apoptosis in oligodendrocytes is directly correlated with demyelination and that inhibition of the apoptosis of oligodendrocytes could be potentially beneficial for recovery after SCI. In the present study, we demonstrated that HGF markedly attenuated the induction of caspase-3 in the oligodendrocytes after SCI, resulting in a significant reduction in the area of demyelination after SCI. Taken together, the antiapoptotic and neurotrophic effects of HGF on the neurons and oligodendrocytes contributed to a significant reduction of the area of parenchymal damage after SCI.

HGF is also well known as a potent angiogenic factor. HGF and c-Met are known to be expressed in endothelial cells and vascular smooth muscle cells (VSMCs; Nakamura et al., 1995, 1996), and a relationship between improved microcirculation and behavioral recovery after cerebral ischemia has been suggested (Shimamura et al., 2004, 2006). A change in the microvasculature of the spinal cord after contusion injury has been shown to be essential for the ability of the spinal cord to undergo self-repair (Loy et al., 2002; Hagg and Oudega, 2006). The cordons of vessels that form early at the lesion site may be the initial stage of the trabeculae described in the contusion injury model; these trabeculae have been reported to promote endogenous repair and support axonal outgrowth in the injured spinal cord (Beattie et al., 1997). Loy and colleagues demonstrated a biphasic angiogenic response after SCI, the first phase of which (3–7 days after injury; Casella et al., 2002), but not the second (28–60 days after injury), corresponded to the time course of functional recovery (Loy et al., 2002). Moreover, a relationship between the blood flow and functional recovery has been shown following strategic treatments to improve angiogenesis in the injured spinal cord during the acute phase of SCI (Glaser et al., 2004; Guizar-Sahagun et al., 2005). Thus, enhancing the formation of blood vessels, especially during the acute phase of SCI, may be a potential repair strategy, because nutritional and mechanical support by vessels is critical

for axonal regeneration. Interestingly, the number, length, and diameter of the vessels have been reported to reach their maximum within 1 week after SCI, and vessels with abnormally large lumina may represent newly formed vessels after SCI (Casella et al., 2002). In the present study, we showed that the introduction of HGF into the injured spinal cord increased the total area of RECA-1-positive endothelial cells and number of vessels with abnormally large lumina by 1 week after SCI, confirming that HGF also promoted angiogenesis during the acute phase of SCI. Because HGF simultaneously stimulates the migration of endothelial cells and VSMCs (Nakamura et al., 1995, 1996), blood vessels might mature in a well-coordinated way, without the release of inflammatory cells (Morishita et al., 2004). Consistently with this suggestion, HGF overexpression reduced cerebral ischemic injury, without causing cerebral edema, through angiogenic and neuroprotective actions (Shimamura et al., 2004). Taken together, our results suggest that HGF may promote angiogenesis without enhancing blood vessel permeability after SCI and contribute to a reduction in the area of damage and regeneration of the injured spinal cord.

Several researchers have reported that HGF plays a role as an axonal chemoattractant and enhances the axonal growth of motoneurons (Ebens et al., 1996; Wong et al., 1997; Caton et al., 2000) and cortical neurons (Yamagata et al., 1995). Furthermore, it has been reported that overexpression of HGF in the chronic stage of cerebral infarction enhances neurite extension and increases the number of synapses, leading to improvements in learning and memory (Shimamura et al., 2006). In the present study, we demonstrated that HGF significantly induced the regrowth of raphe-spinal 5HT-positive fibers, which are known to contribute to the locomotor functions after SCI in rats (Bregman, 1987; Saruhashi et al., 1996; Kim et al., 2004; Kaneko et al., 2006), and the fibers expressed GAP-43 at 6 weeks after SCI. Moreover, c-Met-IR was also detected in the 5HT-positive fibers, suggesting that HGF directly acted on these fibers as well as the neuronal bodies to promote axonal regrwoth and recovery of locomotor functions after SCI. On the other hand, most of the longitudinal RT97-positive fibers oriented parallel to each other (Fig. 7G) did not express GAP-43 but expressed c-Met (Fig. 7J). Because these RT97-positive fibers were observed more abundantly in the HGF group than in the LacZ group at 6 weeks after SCI (Fig. 7H), it is likely that HGF protected the axons from degeneration.

Overall, during the acute phase of SCI, HGF appears to exert significant neuroprotective and antiapoptotic effects, to promote the survival of neurons and oligodendrocytes, and also to enhance angiogenesis around the lesion epicenter after SCI. These effects significantly reduced the area of damage and provided a better scaffold for axonal regeneration. Furthermore, HGF directly acted on the 5HT-positive fibers to promote their regrowth, which likely contributed to the significantly better recovery of the motor functions during the chronic phase of SCI. In conclusion, we have demonstrated that HGF exerted multiple beneficial effects on the injured spinal cord and significantly enhanced endogenous repair after SCI.

ACKNOWLEDGMENTS

We thank Seiji Okada and Hiroyuki Kato for critical review of the manuscript, Tokuko Harada for tender animal care, and Sachiyo Miyao for technical assistance.

REFERENCES

Beattie MS, Bresnahan JC, Komon J, Tovar CA, Van Meter M, Anderson DK, Faden AI, Hsu CY, Noble LJ, Salzman S, Young W. 1997. Endogenous repair after spinal cord contusion injuries in the rat. Exp Neurol 148:453–463.

Blesch A, Tuszynski MH. 2001. GDNF gene delivery to injured adult CNS motor neurons promotes axonal growth, expression of the trophic neuropeptide CGRP, and cellular protection. J Comp Neurol 436:399–410.

Bottaro DP, Rubin JS, Faletto DL, Chan AM, Kmiecik TE, Vande Woude GF, Aaronson SA. 1991. Identification of the hepatocyte growth factor receptor as the c-met protooncogene product. Science 251:802–804.

Bregman BS. 1987. Spinal cord transplants permit the growth of serotonergic axons across the site of neonatal spinal cord transection. Brain Res 431:265–279.

Casella GT, Marcillo A, Bunge MB, Wood PM. 2002. New vascular tissue rapidly replaces neural parenchyma and vessels destroyed by a contusion injury to the rat spinal cord. Exp Neurol 173:63–76.

Caton A, Hacker A, Naeem A, Livet J, Maina F, Bladt F, Klein R, Birchmeier C, Guthrie S. 2000. The branchial arches and HGF are growth-promoting and chemoattractant for cranial motor axons. Development 127:1751–1766.

Coffin RS, Thomas SK, Thomas DP, Latchman DS. 1998. The herpes simplex virus 2 kb latency associated transcript (LAT) leader sequence allows efficient expression of downstream proteins which is enhanced in neuronal cells: possible function of LAT ORFs. J Gen Virol 79:3019–3026.

Date I, Takagi N, Takagi K, Kago T, Matsumoto K, Nakamura T, Takeo S. 2004. Hepatocyte growth factor improved learning and memory dysfunction of microsphere-embolized rats. J Neurosci Res 78:442–453.

Ebens A, Brose K, Leonardo ED, Hanson MG Jr, Bladt F, Birchmeier C, Barres BA, Tessier-Lavigne M. 1996. Hepatocyte growth factor/scatter factor is an axonal chemoattractant and a neurotrophic factor for spinal motor neurons. Neuron 17:1157–1172.

Glaser J, Gonzalez R, Perreau VM, Cotman CW, Keirstead HS. 2004. Neutralization of the chemokine CXCL10 enhances tissue sparing and angiogenesis following spinal cord injury. J Neurosci Res 77:701–708.

Grill R, Murai K, Blesch A, Gage FH, Tuszynski MH. 1997. Cellular delivery of neurotrophin-3 promotes corticospinal axonal growth and partial functional recovery after spinal cord injury. J Neurosci 17:5560–5572.

Guizar-Sahagun G, Ibarra A, Espitia A, Martinez A, Madrazo I, Franco-Bourland RE. 2005. Glutathione monoethyl ester improves functional recovery, enhances neuron survival, and stabilizes spinal cord blood flow after spinal cord injury in rats. Neuroscience 130:639–649.

Hagg T, Oudega M. 2006. Degenerative and spontaneous regenerative processes after spinal cord injury. J Neurotrauma 23:264–280.

Hamanoue M, Takemoto N, Matsumoto K, Nakamura T, Nakajima K, Kohsaka S. 1996. Neurotrophic effect of hepatocyte growth factor on central nervous system neurons in vitro. J Neurosci Res 43:554–564.

Hayashi K, Morishita R, Nakagami H, Yoshimura S, Hara A, Matsumoto K, Nakamura T, Ogihara T, Kaneda Y, Sakai N. 2001. Gene therapy for preventing neuronal death using hepatocyte growth factor: in vivo gene transfer of HGF to subarachnoid space prevents delayed neuronal death in gerbil hippocampal CA1 neurons. Gene Ther 8:1167–1173.

Hisahara S, Yuan J, Momoi T, Okano H, Miura M. 2001. Caspase-11 mediates oligodendrocyte cell death and pathogenesis of autoimmune-mediated demyelination. J Exp Med 193:111–122.

Igawa T, Matsumoto K, Kanda S, Saito Y, Nakamura T. 1993. Hepatocyte growth factor may function as a renotropic factor for regeneration in rats with acute renal injury. Am J Physiol 265:F61–F69.

Ikegami T, Nakamura M, Yamane J, Katoh H, Okada S, Iwanami A, Watanabe K, Ishii K, Kato F, Fujita H, Takahashi T, Okano HJ, Toyama Y, Okano H. 2005. Chondroitinase ABC combined with neural stem/progenitor cell transplantation enhances graft cell migration and outgrowth of growth-associated protein-43-positive fibers after rat spinal cord injury. Eur J Neurosci 22:3036–3046.

Jakeman LB, Wei P, Guan Z, Stokes BT. 1998. Brain-derived neurotrophic factor stimulates hindlimb stepping and sprouting of cholinergic fibers after spinal cord injury. Exp Neurol 154:170–184.

Kaneko S, Iwanami A, Nakamura M, Kishino A, Kikuchi K, Shibata S, Okano HJ, Ikegami T, Moriya A, Konishi O, Nakayama C, Kumagai K, Kimura T, Sato Y, Goshima Y, Taniguchi M, Ito M, He Z, Toyama Y, Okano H. 2006. A selective Sema3A inhibitor enhances regenerative responses and functional recovery of the injured spinal cord. Nat Med 12:1380–1389.

Kim JE, Liu BP, Park JH, Strittmatter SM. 2004. Nogo-66 receptor prevents raphespinal and rubrospinal axon regeneration and limits functional recovery from spinal cord injury. Neuron 44:439–451.

Kobayashi NR, Fan DP, Giehl KM, Bedard AM, Wiegand SJ, Tetzlaff W. 1997. BDNF and NT-4/5 prevent atrophy of rat rubrospinal neurons after cervical axotomy, stimulate GAP-43 and Talpha1-tubulin mRNA expression, and promote axonal regeneration. J Neurosci 17:9583–9595.

Kono S, Nagaike M, Matsumoto K, Nakamura T. 1992. Marked induction of hepatocyte growth factor mRNA in intact kidney and spleen in response to injury of distant organs. Biochem Biophys Res Commun 186:991–998.

Lilley CE, Groutsi F, Han Z, Palmer JA, Anderson PN, Latchman DS, Coffin RS. 2001. Multiple immediate-early gene-deficient herpes simplex virus vectors allowing efficient gene delivery to neurons in culture and widespread gene delivery to the central nervous system in vivo. J Virol 75:4343–4356.

Liu Y, Kim D, Himes BT, Chow SY, Schallert T, Murray M, Tessler A, Fischer I. 1999. Transplants of fibroblasts genetically modified to express BDNF promote regeneration of adult rat rubrospinal axons and recovery of forelimb function. J Neurosci 19:4370–4387.

Loy DN, Crawford CH, Darnall JB, Burke DA, Onifer SM, Whittemore SR. 2002. Temporal progression of angiogenesis and basal lamina deposition after contusive spinal cord injury in the adult rat. J Comp Neurol 445:308–324.

Maina F, Klein R. 1999. Hepatocyte growth factor, a versatile signal for developing neurons. Nat Neurosci 2:213–217.

Matsumoto K, Nakamura T. 1997. Hepatocyte growth factor (HGF) as a tissue organizer for organogenesis and regeneration. Biochem Biophys Res Commun 239:639–644.

Mautes AE, Weinzierl MR, Donovan F, Noble LJ. 2000. Vascular events after spinal cord injury: contribution to secondary pathogenesis. Phys Ther 80:673–687.

McTigue DM, Horner PJ, Stokes BT, Gage FH. 1998. Neurotrophin-3 and brain-derived neurotrophic factor induce oligodendrocyte proliferation and myelination of regenerating axons in the contused adult rat spinal cord. J Neurosci 18:5354–5365.

Miyazawa T, Matsumoto K, Ohmichi H, Katoh H, Yamashima T, Nakamura T. 1998. Protection of hippocampal neurons from ischemia-induced delayed neuronal death by hepatocyte growth factor: a novel neurotrophic factor. J Cereb Blood Flow Metab 18:345–348.

Morishita R, Aoki M, Hashiya N, Yamasaki K, Kurinami H, Shimizu S, Makino H, Takesya Y, Azuma J, Ogihara T. 2004. Therapeutic angiogenesis using hepatocyte growth factor (HGF). Curr Gene Ther 4:199–206.

Nagayama T, Nagayama M, Kohara S, Kamiguchi H, Shibuya M, Katoh Y, Itoh J, Shinohara Y. 2004. Post-ischemic delayed expression of hepatocyte growth factor and c-Met in mouse brain following focal cerebral ischemia. Brain Res 999:155–166.

Nakamura T, Nawa K, Ichihara A. 1984. Partial purification and characterization of hepatocyte growth factor from serum of hepatectomized rats. Biochem Biophy Res Commun 122:1450–1459.

Nakamura T, Nishizawa T, Hagiya M, Seki T, Shimonishi M, Sugimura A, Tashiro K, Shimizu S. 1989. Molecular cloning and expression of human hepatocyte growth factor. Nature 342:440–443.

Nakamura Y, Morishita R, Higaki J, Kida I, Aoki M, Moriguchi A, Yamada K, Hayashi S, Yo Y, Matsumoto K, et al. 1995. Expression of local hepatocyte growth factor system in vascular tissues. Biochem Biophys Res Commun 215:483–488.

Nakamura Y, Morishita R, Nakamura S, Aoki M, Moriguchi A, Matsumoto K, Nakamura T, Higaki J, Ogihara T. 1996. A vascular modulator, hepatocyte growth factor, is associated with systolic pressure. Hypertension 28:409–413.

Niimura M, Takagi N, Takagi K, Mizutani R, Ishihara N, Matsumoto K, Funakoshi H, Nakamura T, Takeo S. 2006. Prevention of apoptosis-inducing factor translocation is a possible mechanism for protective effects of hepatocyte growth factor against neuronal cell death in the hippocampus after transient forebrain ischemia. J Cereb Blood Flow Metab (in press).

Noji S, Tashiro K, Koyama E, Nohno T, Ohyama K, Taniguchi S, Nakamura T. 1990. Expression of hepatocyte growth factor gene in endothelial and Kupffer cells of damaged rat livers, as revealed by in situ hybridization. Biochem Biophys Res Commun 173:42–47.

Okura Y, Arimoto H, Tanuma N, Matsumoto K, Nakamura T, Yamashima T, Miyazawa T, Matsumoto Y. 1999. Analysis of neurotrophic effects of hepatocyte growth factor in the adult hypoglossal nerve axotomy model. Eur J Neurosci 11:4139–4144.

Palmer JA, Branston RH, Lilley CE, Robinson MJ, Groutsi F, Smith J, Latchman DS, Coffin RS. 2000. Development and optimization of herpes simplex virus vectors for multiple long-term gene delivery to the peripheral nervous system. J Virol 74:5604–5618.

Ramon-Cueto A, Plant GW, Avila J, Bunge MB. 1998. Long-distance axonal regeneration in the transected adult rat spinal cord is promoted by olfactory ensheathing glia transplants. J Neurosci 18:3803–3815.

Saruhashi Y, Young W, Perkins R. 1996. The recovery of 5-HT immunoreactivity in lumbosacral spinal cord and locomotor function after thoracic hemisection. Exp Neurol 139:203–213.

Shimamura M, Sato N, Oshima K, Aoki M, Kurinami H, Waguri S, Uchiyama Y, Ogihara T, Kaneda Y, Morishita R. 2004. Novel therapeutic strategy to treat brain ischemia: overexpression of hepatocyte growth factor gene reduced ischemic injury without cerebral edema in rat model. Circulation 109:424–431.

Shimamura M, Sato N, Waguri S, Uchiyama Y, Hayashi T, Iida H, Nakamura T, Ogihara T, Kaneda Y, Morishita R. 2006. Gene transfer of hepatocyte growth factor gene improves learning and memory in the chronic stage of cerebral infarction. Hypertension 47:742–751.

Sun W, Funakoshi H, Matsumoto K, Nakamura T. 2000. A sensitive quantification method for evaluating the level of hepatocyte growth factor and c-met/HGF receptor mRNAs in the nervous system using competitive RT-PCR. Brain Res Brain Res Protoc 5:190–197.

Tamura M, Nakamura M, Ogawa Y, Toyama Y, Miura M, Okano H. 2005. Targeted expression of anti-apoptotic protein p35 in oligodendrocytes reduces delayed demyelination and functional impairment after spinal cord injury. Glia 51:312–321.

Tuszynski MH, Peterson DA, Ray J, Baird A, Nakahara Y, Gage FH. 1994. Fibroblasts genetically modified to produce nerve growth factor induce robust neuritic ingrowth after grafting to the spinal cord. Exp Neurol 126:1–14.

Tuszynski MH, Gabriel K, Gage FH, Suhr S, Meyer S, Rosetti A. 1996. Nerve growth factor delivery by gene transfer induces differential outgrowth of sensory, motor, and noradrenergic neurites after adult spinal cord injury. Exp Neurol 137:157–173.

Vavrek R, Girgis J, Tetzlaff W, Hiebert GW, Fouad K. 2006. BDNF promotes connections of corticospinal neurons onto spared descending interneurons in spinal cord injured rats. Brain 129:1534–1545.

Wong V, Glass DJ, Arriaga R, Yancopoulos GD, Lindsay RM, Conn G. 1997. Hepatocyte growth factor promotes motor neuron survival and synergizes with ciliary neurotrophic factor. J Biol Chem 272:5187–5191.

Yamagata T, Muroya K, Mukasa T, Igarashi H, Momoi M, Tsukahara T, Arahata K, Kumagai H, Momoi T. 1995. Hepatocyte growth factor specifically expressed in microglia activated Ras in the neurons, similar to the action of neurotrophic factors. Biochem Biophys Res Commun 210:231–237.

Yanagita K, Matsumoto K, Sekiguchi K, Ishibashi H, Niho Y, Nakamura T. 1993. Hepatocyte growth factor may act as a pulmotrophic factor on lung regeneration after acute lung injury. J Biol Chem 268:21212–21217.

Zhao MZ, Nonoguchi N, Ikeda N, Watanabe T, Furutama D, Miyazawa D, Funakoshi H, Kajimoto Y, Nakamura T, Dezawa M, Shibata MA, Otsuki Y, Coffin RS, Liu WD, Kuroiwa T, Miyatake S. 2006. Novel therapeutic strategy for stroke in rats by bone marrow stromal cells and ex vivo HGF gene transfer with HSV-1 vector. J Cereb Blood Flow Metab 26:1176–1188.

Development/Plasticity/Repair

In Vivo Tracing of Neural Tracts in the Intact and Injured Spinal Cord of Marmosets by Diffusion Tensor Tractography

Kanehiro Fujiyoshi,[1,2]* Masayuki Yamada,[4,5]* Masaya Nakamura,[1] Junichi Yamane,[1,2] Hiroyuki Katoh,[1] Kazuya Kitamura,[1,2] Kenji Kawai,[4] Seiji Okada,[6] Suketaka Momoshima,[3] Yoshiaki Toyama,[1] and Hideyuki Okano[2]

Department of [1]Orthopaedic Surgery, [2]Physiology, and [3]Radiology and [4]Center for Integrated of Medical Research, Keio University School of Medicine, Shinjuku, Tokyo 160-8582, Japan, [5]Central Institute for Experimental Animals, Miyamae-ku, Kawasaki, Kanagawa 216-0001, Japan, and [6]Department of Research Superstar Program Stem Cell Unit, Graduate School of Medical Science, Kyushu University, Fukuoka 812-8582, Japan

In spinal cord injury, axonal disruption results in motor and sensory function impairment. The evaluation of axonal fibers is essential to assess the severity of injury and efficacy of any treatment protocol, but conventional methods such as tracer injection in brain parenchyma are highly invasive and require histological evaluation, precluding clinical applications. Previous advances in magnetic resonance imaging technology have led to the development of diffusion tensor tractography (DTT) as a potential modality to perform *in vivo* tracing of axonal fibers. The properties and clinical applications of DTT in the brain have been reported, but technical difficulties have limited DTT studies of the spinal cord. In this study, we report the effective use of DTT to visualize both intact and surgically disrupted spinal long tracts in adult common marmosets. To verify the feasibility of spinal cord DTT, we first performed DTT of postmortem marmosets. DTT clearly illustrated spinal projections such as the corticospinal tract and afferent fibers in control animals, and depicted the severed long tracts in the injured animals. Histology of the spinal cords in both control and injured groups were consistent with DTT findings, verifying the accuracy of DTT. We also conducted DTT in live marmosets and demonstrated that DTT can be performed in live animals to reveal *in vivo* nerve fiber tracing images, providing an essential tool to evaluate axonal conditions in the injured spinal cord. Taken together, these findings demonstrate the feasibility of applying DTT to preclinical and clinical studies of spinal cord injury.

Key words: spinal cord injury; corticospinal tract; diffusion tensor tractography; magnetic resonance imaging; common marmoset; calmodulin-dependent protein kinase II-α; pathway-specific DTT; *in vivo* tracing

Introduction

We established previously a reproducible spinal cord injury (SCI) model in adult common marmosets and demonstrated that transplantation of human neural stem/progenitor cells into the injured spinal cord promoted functional recovery (Iwanami et al., 2005b). An increase of axonal fibers, evaluated through histological methods, was observed near the transplanted neural stem/progenitor cells and were interpreted to be involved in the functional improvement. Such evaluation of axonal fibers is essential to assess the severity of SCI and efficacy of any treatment protocol (Olson, 2002; Kaneko et al., 2007), but conventional methods such as tracer injection in brain parenchyma are technically demanding and highly invasive (Ralston and Ralston, 1985; Lacroix et al., 2004). Because histological examinations are required to evaluate tracer studies, it has been impossible to evaluate axonal fibers *in vivo* and follow the sequential growth of axonal fibers in the same animal. Understanding the value of such an examination method, we therefore sought to establish a noninvasive method to evaluate axonal fibers *in vivo*.

Magnetic resonance imaging (MRI) is essential for predicting prognosis and planning the treatment of patients with SCI (Kulkarni et al., 1987; Yamashita et al., 1990). Our previous study using common marmosets also demonstrated that MRI could detect pathological changes after SCI (Iwanami et al., 2005a). However, the information provided by conventional T1- and T2-weighted MRI of the spinal cord is essentially limited to the differentiation of the white matter from the gray matter. Conventional MRI depicts the white matter as a uniform tissue, although it actually contains a complex array of directionally oriented nerve fibers. Methods to visualize the pathways of the white matter *in vivo* have been long sought and, recently, diffusion tensor tractography (DTT) has demonstrated this ability (Ito et al., 2002; Masutani et al., 2003; Mori et al., 2003).

Diffusion tensor imaging (DTI) is a new imaging technique that takes advantage of the anisotropic nature of water diffusion in biological tissue to obtain detailed microstructural information (Le Bihan et al., 1986; Moseley et al., 1990; Basser et al., 1994; Beaulieu, 2002; Mori and Zhang, 2006). By analyzing and reconstructing that data obtained by DTI, DTT can follow the orienta-

Received July 24, 2007; accepted Sept. 4, 2007.

This work was supported by grants from the Leading Project for Realization of Regenerative Medicine from the Ministry of Education, Culture, Sports, Science and Technology (MEXT) of Japan, from the Japan Science and Technology Corporation, from the General Insurance Association, and by a grant-in-aid from the 21st Century COE Program of MEXT, Japan, to Keio University. We thank Hirotaka James Okano and Ichio Aoki for critical review of this manuscript, Humika Toyoda for tender animal care, and Ai Yokokawa for technical assistance.

*K.F. and M.Y. contributed equally to this work.

The authors declare no competing financial interests.

Correspondence should be addressed to Hideyuki Okano, 35 Shinanomachi, Shinjuku-ku, Tokyo 160-8582, Japan. E-mail: hidokano@sc.itc.keio.ac.jp.

DOI:10.1523/JNEUROSCI.3354-07.2007

 0270-6474/07/2711991-08$15.00/0

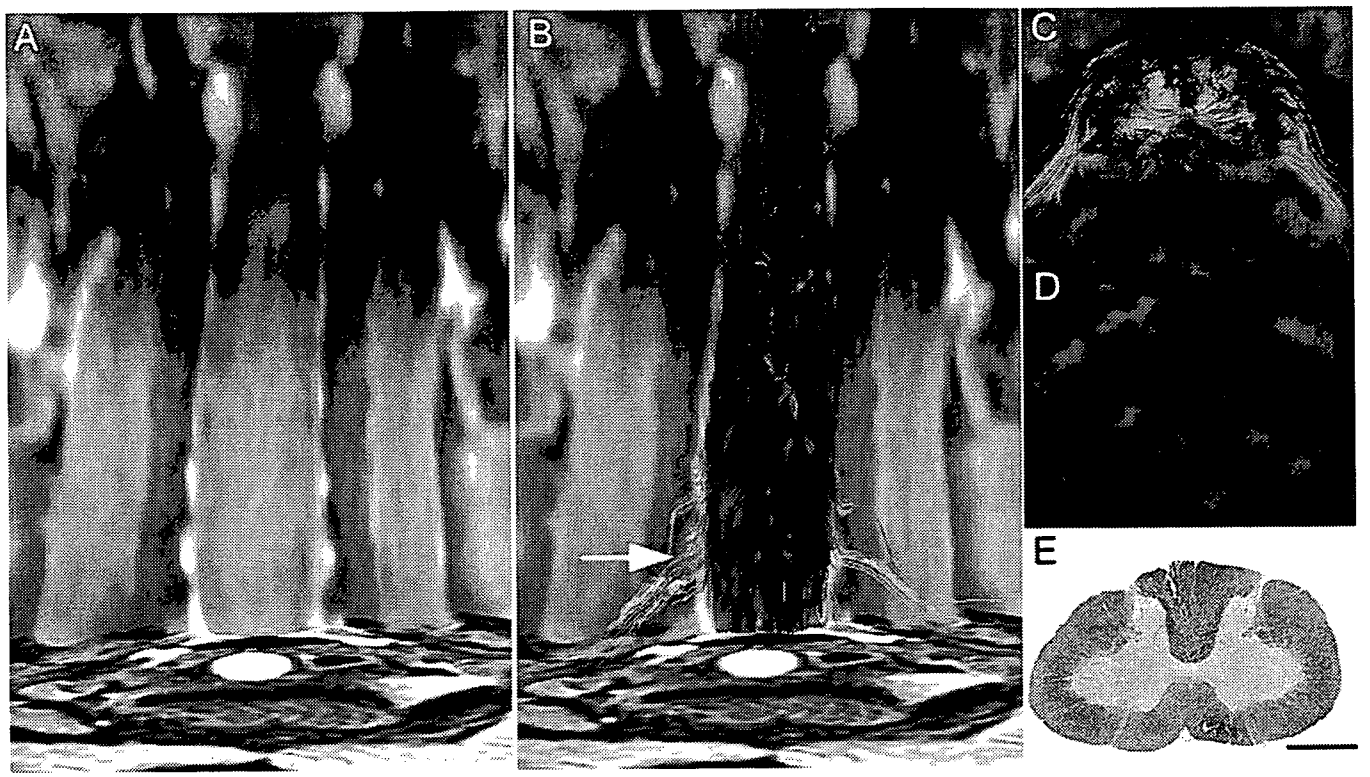

Figure 1. DTT of the intact spinal cord in a postmortem common marmoset. ***A***, Coronal T2-weighted MRI. ***B***, ***C***, Full-width DTT of the spinal cord (***B***) and an axial section (***C***) superimposed on axial T2-weighted images. The ROI was placed in the lower cervical spinal cord and DTT was traced in the cranial direction. DTT tracts are color coded to indicate tract orientation: red for left–right orientation, green for anterior–posterior orientation, and blue for superior–inferior orientation. ***D***, ***E***, Directionally color-coded axial FA map of the spinal cord (***D***) reveals that the configuration of the white matter depicted in blue is consistent with the myelin-positive area in an axial section of the same area stained with LFB (***E***). ***C–E*** are axial images of the C5/6 level (***B***, arrow). Scale bar, 1 mm.

tion of nerve fibers to trace specific neural pathways such as the corticospinal tract (CST) in the brain (Conturo et al., 1999; Masutani et al., 2003; Kamada et al., 2005a; Lee et al., 2005). Compared with the brain, however, DTT of the spinal cord is more difficult because of its smaller size and *in vivo* bulk motion (Basser and Jones, 2002; Maier and Mamata, 2005; Kharbanda et al., 2006). Several researchers have reported previously on successful DTT of the human spinal cord (Holder et al., 2000; Facon et al., 2005; Tsuchiya et al., 2005; Ducreux et al., 2006). However, because these DTT images were not confirmed with detailed histological studies, whether DTT actually reflects the anatomical axonal fibers remains unclear. In this study, we performed DTT of both intact and injured spinal cords in common marmosets and confirmed the accuracy of DTT through histology.

Materials and Methods

Hemisection SCI in common marmoset. Adult female common marmosets (266–384 g; Clea Japan, Tokyo, Japan) were used in the present study ($n = 6$). All interventions and animal care procedures were performed in accordance with the Laboratory Animal Welfare Act, the *Guide for the Care and Use of Laboratory Animals* (National Institutes of Health), and the *Guidelines and Policies for Animal Surgery* provided by the Animal Study Committee of the Central Institute for Experimental Animals of Keio University, and were approved by the ethics committee of Keio University. All surgeries were performed under general anesthesia induced by intramuscular injection of ketamine (50 mg/kg; Sankyo, Tokyo, Japan) and xylazine (5 mg/kg; Bayer, Leverkusen, Germany) and maintained by isoflurane (Foren; Abbott, Tokyo, Japan). The animal's pulse, arterial oxygen saturation, and rectal temperature were monitored during the surgical procedures. After a laminectomy at the C6 level, the dura mater was opened longitudinally and the right side of the spinal cord was cut at the C6 level using a surgical scalpel in the hemisection group ($n = 3$). The control group in this study in was a naive control without any surgical intervention.

Magnetic resonance imaging. MRI was performed using a 7.0 tesla MRI, PharmaScan 70/16 (BioSpin; Bruker) with a coil dedicated for small animals. In the studies using postmortem animals (control and hemisection groups, $n = 2$ each), conventional T2-weighted images (T2WIs) were first obtained, followed by intracardiac perfusion with 4% paraformaldehyde (PFA), pH 7.4, and diffusion tensor MRI. T2WI and diffusion tensor MRI of the hemisected animals were conducted 2 weeks after injury. DTI data sets were acquired with a spin-echo sequence based on the Stejskal–Tanner diffusion preparation. Scanning parameters were as follows: repetition time (TR), 15000 ms; echo time (TE), 40 ms; flip angle, 90°, field of view (FOV), 55 × 55 mm; acquisition data matrix, 256 × 256; reconstructed image resolution, 0.215 mm (with zero-filling interpolation); slice thickness, 0.85 mm; b-value, 1000 s/mm^2; motion-probing gradient (MPG) orientations, 12 axes; number of averaging (NA), 1. In the studies using live animals (control and hemisection group, $n = 1$ each), conventional and diffusion tensor MRI were performed under the general anesthesia as mentioned above. MRI scans of the hemisected animal were conducted 2 weeks after injury. In live animals, to reduce motion artifacts from the blood flow and CSF flow, animals were immobilized on an acrylic bed with a specially designed head positioner and electrocardiogram (ECG) probe (SA Instruments) for gated imaging was attached to the animal's front thorax. DTI data sets in live animals were acquired with an ECG-gated standard diffusion weighted spin-echo pulse sequence based on the Stejskal–Tanner diffusion preparation (Stejskal and Tanner, 1965). Scanning parameters were as follows: TR, 3500 ms; TE, 40 ms; flip angle, 90°; FOV, 40 × 40 mm; acquisition data matrix, 128 × 128; reconstructed image resolution, 0.31 × 0.31 mm; slice thickness, 0.94 mm; b-value, 1000 s/mm^2; MPG orientations, 12 axes; NA, 1.

Diffusion tensor analysis. Diffusion tensor and three-dimensional analysis were performed using Volume One and dTVIISR software (Kuni-

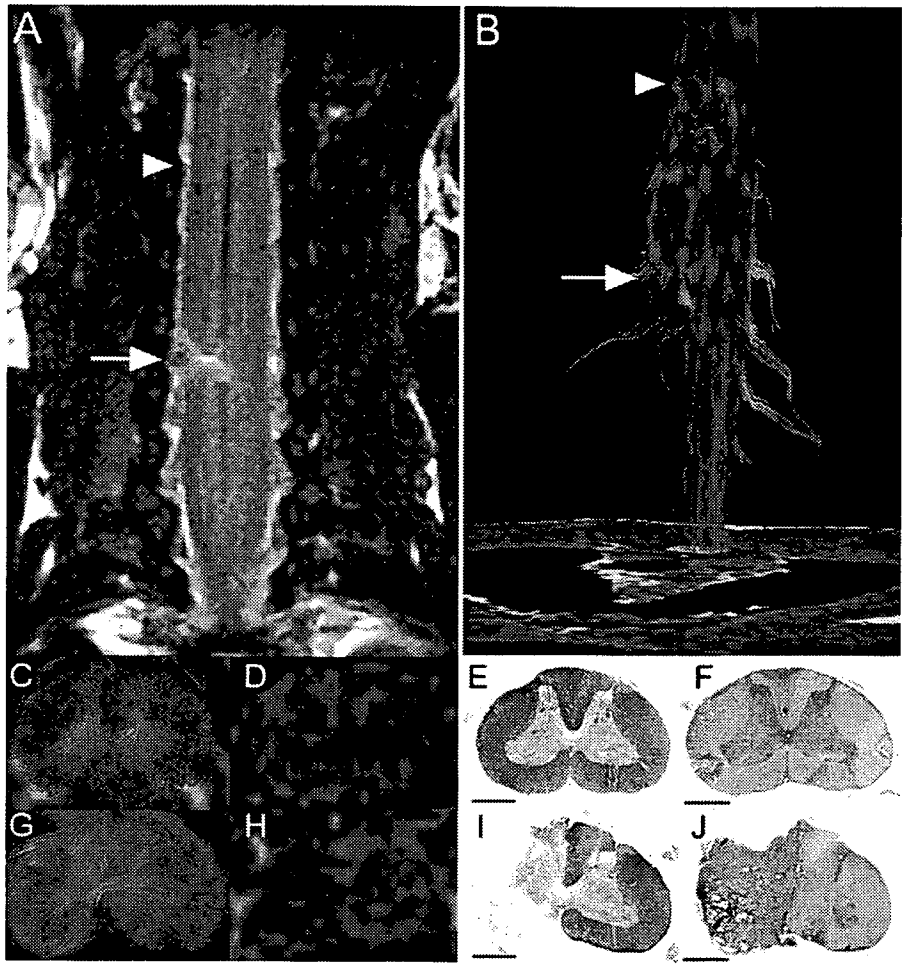

Figure 2. DTT of the hemisected spinal cord at 2 weeks after injury in a postmortem common marmoset. ***A***, Coronal T2-weighted MRI depicted the hemisection injury as a low-intensity area with no change in the cord caudal to the injury. ***B***, DTT of the hemisected spinal cord. The ROI was placed in the upper cervical spinal cord, and DTT was traced in the caudal direction revealing disruption of white matter fibers on the hemisected side. The traced tracts became untraceable at the injury site, whereas tracts on the contralateral side continued caudally. Arrows indicated the hemisection site and arrowheads indicated the point 8 mm cranial to the injury site in ***A*** and ***B***. ***C–J***, DTT (***C***, ***G***), FA map (***D***, ***H***), LFB staining (***E***, ***I***), and HE staining (***F***, ***J***) of the spinal cord 8 mm cranial to the injury site (***C–F***) and at the hemisection site (***G–J***). Although normal FA and anatomy of the spinal cord was confirmed cranial to the hemisection site, there was a significant decrease in FA of the white matter fibers at the hemisection site (***G***, ***H***). Consistent with these changes in DTT (***G***) and color-coded FA map (***H***), demyelination was seen at the hemisection site (***I***). Scale bars, 1 mm.

matsu et al., 2003; Masutani et al., 2003). An eigenvector ($e1$) associated with the largest eigenvalue ($\lambda 1$) was assumed to represent the local fiber direction. Fiber tracking was initiated from a manually selected region of interest (ROI) area, which is the "seed" from which tracking lines were propagated bidirectionally according to the eigenvector ($e1$) at each voxel pixel. The direction of diffusion anisotropy was followed until tracking was terminated when it reached a voxel with a fractional anisotropy of <0.25. To delineate the motor tracts, the seed was placed on the area histologically known to contain CaMKII-α-positive fibers in the upper cervical cord, which corresponds to the CST (Terashima et al., 1994; Iwanami et al., 2005a). To delineate the afferent pathways of the spinal cord, we placed the seed at the anterolateral and posterior funiculi of the lower cervical cord, which correspond to the spinothalamic tract and the gracile fasciculus, respectively. We used the two-regions-of-interest method (Mori et al., 2003), which consists of seed and target regions to depict the pyramidal decussation from the medullary pyramid (seed) to the opposite CST area in the upper cervical cord (target).

Histological analyses. In the postmortem group, spinal cord tissues were removed after diffusion tensor MRI. In the live group, each animal was perfused intracardially with 4% paraformaldehyde after diffusion tensor MRI and then the spinal cord tissues were removed. All spinal cord specimens were postfixed in 4% PFA and immersed overnight in 10% sucrose followed by 30% sucrose. Frozen section blocks were prepared and cut into 20-μm-thick axial sections using a cryostat. These sections were stained with hematoxylin-eosin (HE) for general histological examinations and Luxol fast blue (LFB) for evaluation of the myelinated area. Immunostaining with anti-CaMKII-α antibody (primary antibody, diluted 1:100, mouse monoclonal; Zymed, San Francisco, CA; secondary antibody, a biotin-labeled goat anti-mouse IgG for ABC and DAB staining) was performed to examine the CST.

Results

DTT of intact and injured spinal cords in postmortem common marmosets

Based on the data from *in vivo* high-resolution diffusion tensor MR images of postmortem common marmoset spinal cords (Fig. 1*A*), we created a DTT of the cervical spinal cord that enabled us to detect various fibers of the spinal cord (Fig. 1*B*). In a color-coded DTT of the intact cervical spinal cord, each path traced by DTT, which we will refer to have as a tract, is depicted in colors according to its orientation (Pajevic and Pierpaoli, 1999): red for left–right orientation, green for anterior–posterior orientation, and blue for superior–inferior orientation (Fig. 1*B*,*C*). White matter fibers with high craniocaudal diffusion anisotropy were visible in blue on color-coded maps of fractional anisotropy (FA) (Basser and Pierpaoli, 1996), an index of anisotropy ranging from 0 (perfectly isotropic diffusion) to 1 (a hypothetical infinite cylinder), which had been calculated from the same data (Fig. 1*D*) and the distribution of longitudinal fibers was consistent with the distribution of myelinated axons stained with LFB (Fig. 1*E*). In the gray matter, horizontal fibers passing from the central canal to the anterior horn of the spinal cord were observed in red, but almost no diffusion anisotropy was detected in the remaining gray matter, which is mainly occupied by neuronal and glial cells.

In the marmosets with hemisected spinal cords, the hemisected area of spinal cord appeared as a high-intensity area in coronal T2WIs 2 weeks after injury (Fig. 2*A*). DTT of the hemisected spinal cord revealed that the longitudinal fibers of the white matter in the injured side were disrupted at the hemisection site, but preserved in the intact side (Fig. 2*B*). In axial DTT images and color-coded FA maps, there was a significant decrease in FA of the longitudinal fibers of the white matter as well as the transverse fibers of the gray matter at the hemisection site (Fig. 2*G*,*H*), compared with the site 8 mm cranial to the hemisection site (Fig. 2*C*,*D*). Consistent with these changes in DTT and colored FA maps, histology of the hemisected area revealed disruption of both gray and white matter with severe demyelination. (Fig. 2*I*,*J*).

Pathway-specific DTT in postmortem common marmosets

To examine the feasibility of visualizing individual pathways in common marmosets, we analyzed the CST from the medulla to the upper cervical spinal cord because the course of the CST in this region is unique and well known. Analysis of histological sections stained for calmodulin-dependent protein kinase II-α (CaMKII-α) determined the location of the CST (Terashima et al., 1994; Iwanami et al., 2005a) within the medulla, and DTT of the CST was performed by setting the ROI, which is a manually selected area based on anatomical knowledge from which DTT fiber tracking was initiated, in the pyramid of the medulla and tracing caudally (Fig. 3*A*). The course of the CST in this area has been well documented in the literature; the majority of fibers cross to the contralateral side through the pyramidal decussation and descended the lateral funiculus (lateral CST), whereas a small group of fibers descend the ipsilateral anterior (anterior CST) and lateral funiculus (anterolateral CST) (Qiu et al., 1991; Lacroix et al., 2004; Lemon et al., 2004). A study in humans demonstrated the composition of the CST, with the lateral CST accounting for 90% of CST fibers and the anterior CST and uncrossed lateral CST accounting for the remaining 8 and 2%, respectively (Carpenter and Sutin, 1983). DTT was capable of tracing fibers through all three courses and successfully demonstrated the pyramidal decussation of the CST (Fig. 3*B–E*). However the number of tracts depicted with DTT through each course did not reflect the amount of CST fibers traveling through each pathway, because the number of DTT tracts depicted descending each pathway were similar although a majority of CST fibers actually travel through the lateral CST.

We focused on the pyramidal decussation of the CST and conducted histological studies to verify the results of DTT. DTT and histological sections from similar points along the craniocaudal axis were compared. The course of the CST depicted by DTT (Fig. 3*H*) corresponded to the area positive for CaMKII-α (Fig. 3*I*), which recognizes fibers of the CST, and LFB staining of the same section (Fig. 3*J*) confirmed that the CST delineated by DTT and CaMKII-α contained myelinated fibers. CST-specific DTT superimposed on MR images verified that the pyramidal decussation was depicted in the proper position (Fig. 3*F*,*G*).

With sufficient data to indicate that CST-specific DTT is possible, we then con-

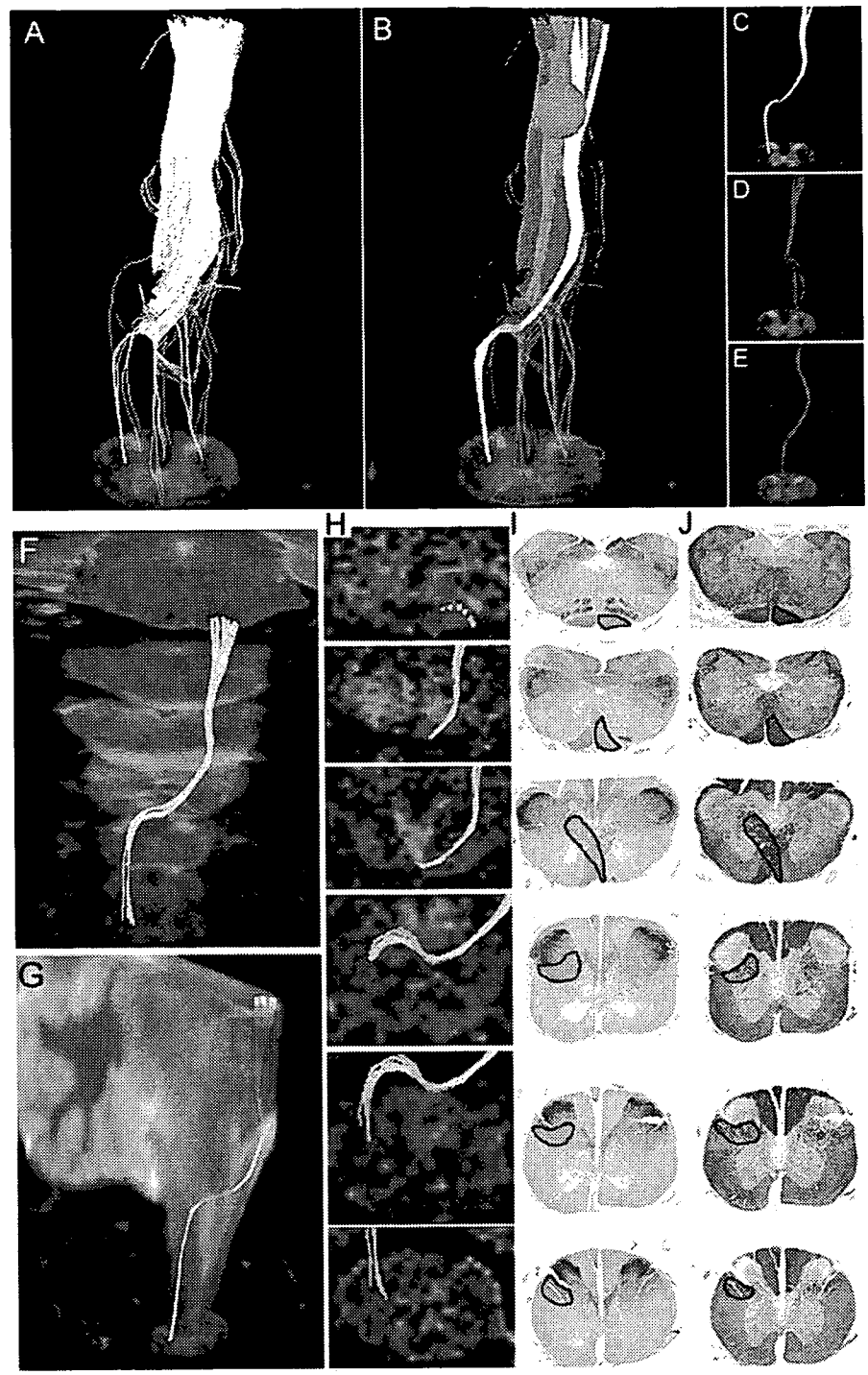

Figure 3. Pathway-specific DTT in a postmortem common marmoset revealing the course of the corticospinal tract with pyramidal decussation. ***A***, DTT of the CST was conducted by placing the ROI in the pyramid of the medulla and tracing caudally. Note that the volume of traced tracts decrease as the tracing was carried caudally, because many tracts became untraceable because of the partial volume effect. ***B***, By placing secondary ROIs in areas of the upper cervical spinal cord known to contain CST fibers, CST fibers that pass through both ROIs could be depicted. ***C***, Lateral CST fibers that crossed over to and descended the contralateral lateral funiculus in a pattern suggesting pyramidal decussation were depicted in yellow. ***D***, Uncrossed lateral fibers descending the ipsilateral lateral funiculus were depicted in red. ***E***, Lateral fibers descending the ipsilateral anterior funiculus were depicted in blue. The fact that DTT was capable of accurately depicting all three known pathways of the CST is significant. However, it is important to note that the depicted DTT tracts do not accurately reflect the volume of nerve fibers, because it is known that the lateral CST contains the majority of CST fibers. ***F***, ***G***, DTT of the pyramidal decussation superimposed on three-dimensional MR images to macroscopically confirm that the pyramidal decussation was depicted in the proper height in the medulla and the upper cervical cord, using the cerebellum as a reference point. ***H***, DTT of the pyramidal decussation superimposed on axial color-coded FA maps. ***I***, ***J***, Axial histological slices of the same points in ***H*** stained for CaMKII-α to reveal the location of CST fibers (***I***) and LFB to delineate the configuration of the white matter (***J***). In each slice, the area through which the DTT CST tract passes was positive for CaMKII-α and LFB, confirming the accuracy of DTT.

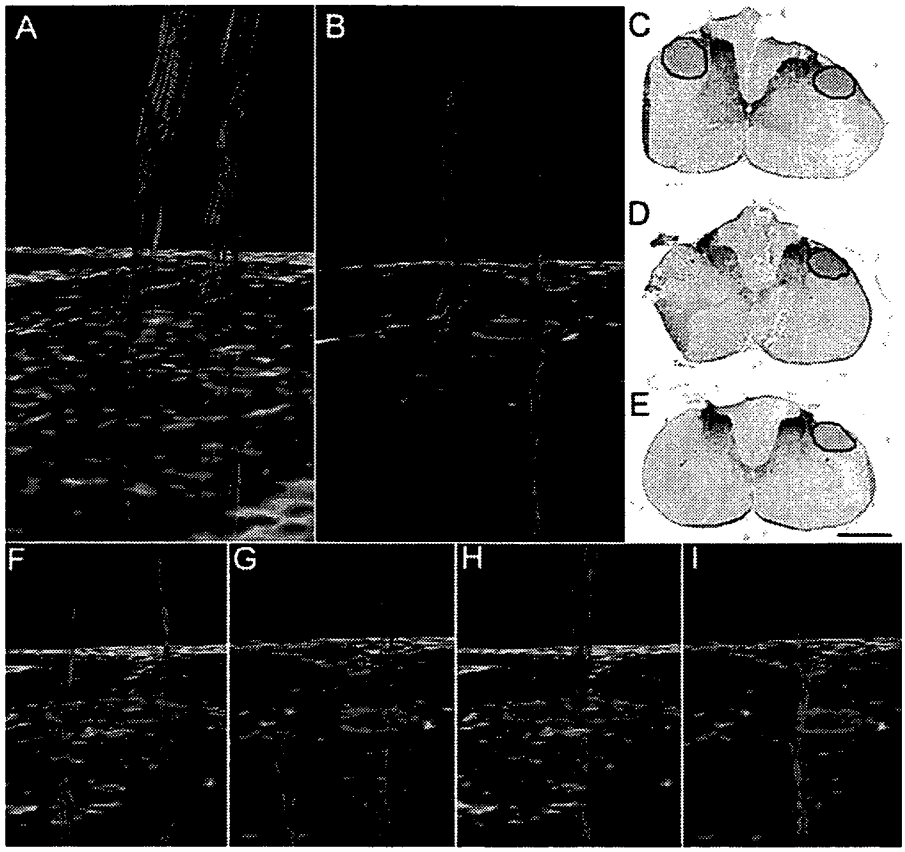

Figure 4. *In vivo* CST- and afferent pathway-specific DTT of intact and injured spinal cords in postmortem common marmosets. ***A***, DTT of an intact CST superimposed on a color-coded FA map of the C5/6 level. ***B***, DTT of the CST in a hemisected spinal cord superimposed on a color-coded FA map of the hemisected C5/6 level 2 weeks after injury revealing disruption of the CST at the site of injury. ***C–E***, CaMKII-α staining of an axial section of the hemisected spinal cord 8 mm cranial to the hemisection site (***C***), at the hemisection site (***D***), and 8 mm caudal to the hemisection site (***E***). Because CaMKII-α is a known substance transported in the axons of the CST, the absence of CaMKII-α staining distal to the injury suggested CST disruption, confirming the results of CST-specific DTT. ***F***, ***H***, In the control group, ROI was placed at the anterolateral funiculus (***F***) or the posterior funiculus (***H***), and a DTT of the afferent pathways was drawn in the caudocranial direction. ***G***, ***I***, In the hemisection group, no fibers were observed at the site rostral to the hemisection site, demonstrating that tract-specific DTT can potentially delineate the spinothalamic tract (***G***) and dorsal column-medial lemniscus pathway (***I***). Scale bar, 1 mm.

ducted CST-specific DTT of hemisected spinal cords to observe how DTT would depict an injured pathway. CST-specific DTTs of the middle to lower cervical spinal cord were compared in intact and hemisected postmortem common marmosets. In the intact cervical spinal cord, DTT depicted descending CST tracts in the bilateral lateral funiculus (Fig. 4*D*). In the hemisected cervical spinal cord 2 weeks after injury, FA decreased in color-coded FA maps and no tracts were found caudal to the hemisection site on the injured side whereas the intact CST pathway was observed descending the uninjured side (Fig. 4*B*). Histology confirmed the disruption of the CST at the hemisection site with robust CaMKII-α staining rostral to the hemisection (Fig. 4*C*) and no CaMKII-α positive CST fibers at and caudal to the hemisection site (Fig. 4*D*,*E*).

Using a similar technique, it is also possible to trace pathways other than the CST. By placing the ROI in areas known to contain afferent fibers and tracing in the caudocranial direction, the spinothalamic tract in the anterolateral funiculus (Fig. 4*F*) and the medial lemniscus pathway in the posterior funiculus (Fig. 4*B*) were depicted. When the same procedure was repeated in the hemisected group, the ascending tracts were disrupted at the hemisection site with no tracts rostral to the lesion on the injured side, whereas normal ascending tracts were observed in the uninjured side (Fig. 4*G*,*I*).

Pathway-specific DTT of intact and injured spinal cords in live common marmosets

To evaluate the clinical feasibility of DTT, we repeatedly performed *in vivo* pathway-specific DTT on live animals and compared the results with those obtained from postmortem animals. Similar to the DTT of postmortem animals, *in vivo* DTT of the intact cervical CST in live animals showed longitudinal tracts in the lateral funiculus bilaterally (Fig. 5*B*), and pathway-specific DTT of afferent fibers depicted tracts in the anterolateral and posterior funiculus (Figs. 5*C*,*D*). In the hemisected marmoset 2 weeks after injury, T2WI MRI revealed a low-intensity area at the hemisection site and a high-intensity area at the same level on the intact side (Fig. 5*E*), whereas DTT showed disruption of the CST (Fig. 5*F*) and ascending fibers at the lesion site (Fig. 5*G*,*H*). Pathway-specific *in vivo* DTT findings in live animals were highly similar to those of postmortem animals, especially in major tract morphology. Because MRI scans of live animals required anesthesia, the scan duration and, therefore, scan area were considerably limited compared with postmortem animals; MRIs of live animals were conducted in 1.5 h whereas 10 h scans were performed for postmortem animals. Overall, these findings demonstrated that it is feasible to depict the descending and ascending pathways of the spinal cord in live animals using pathway-specific DTT, and demonstrate the usefulness of DTT as an imaging method to assess specific pathways in spinal cord injuries.

Discussion

Because we hope to clinically apply this procedure to human SCI patients in the future, common marmosets were selected for this study. As primates, they are closely related to humans in terms of neurofunctional anatomy of the spinal cord. For example, the CST fibers localize mainly in the dorsal funiculus in rodents, whereas in primates they are mainly located in the lateral funiculus (Qiu et al., 1991; Terashima et al., 1994; Lacroix et al., 2004; Lemon et al., 2004; Iwanami et al., 2005a). From a practical standpoint, common marmosets are easy to handle, breed effectively, and are small enough to fit into the narrow MRI coil.

In our past studies of SCI in common marmosets, we have used contusion injury models because, compared with other SCI methods, contusion injuries more closely resemble the pathological conditions found in human SCI patients (Iwanami et al., 2005a,b). In this study, however, we chose a hemisection model because the disruption and regeneration of axons after a hemisection injury is easier to evaluate than a contusion injury (Levi et al., 2002; Tuszynski et al., 2002). Because the main objective of this study was to evaluate the usefulness of DTT in assessing axonal